



Calibration of NOMAD on ESA's ExoMars Trace Gas Orbiter: Part 2 – The Limb, Nadir and Occultation (LNO) channel



Ian R. Thomas^{a,*}, Shohei Aoki^{a,b}, Loïc Trompet^a, Séverine Robert^{a,c}, Cédric Depiesse^a, Yannick Willame^a, Guillaume Cruz-Mermy^d, Frédéric Schmidt^d, Justin T. Erwin^a, Ann Carine Vandaele^a, Frank Daerden^a, Arnaud Mahieux^a, Eddy Neefs^a, Bojan Ristic^a, Laszlo Hetey^a, Sophie Berkenbosch^a, Roland Clairquin^a, Bram Beeckman^a, Manish R. Patel^{e,f}, Jose Juan Lopez-Moreno^g, Giancarlo Bellucci^h, the NOMAD Team

^a Royal Belgian Institute for Space Aeronomy (BIRA-IASB), Av. Circulaire 3, 1180, Brussels, Belgium

^b Institute of Space and Astronautical Science (ISAS), Japan Aerospace Exploration Agency (JAXA), 3-1-1 Yoshinodai, Sagami-hara, Kanagawa, 252-5210, Japan

^c Institute of Condensed Matter and Nanosciences, Université Catholique de Louvain, Chemin du Cyclotron 2, 1348, Louvain-la-Neuve, Belgium

^d Université Paris Saclay, Géosciences Paris Saclay, 91405, Orsay, France

^e The Open University, Walton Hall, Milton Keynes, MK7 6AA, UK

^f STFC Rutherford Appleton Laboratory, Oxfordshire, OX11 0QX, UK

^g Instituto de Astrofísica de Andalucía (IAA/CSIC), Granada, Spain

^h Istituto di Astrofisica e Planetologia Spaziali (IAPS/INAF), Via del Fosso del Cavaliere, 00133, Rome, Italy

ARTICLE INFO

Keywords:

Mars atmosphere
Infrared spectroscopy
Nadir viewing
Calibration
Trace gas orbiter

ABSTRACT

The Nadir and Occultation for Mars Discovery (NOMAD) instrument is a 3-channel spectrometer suite on the ESA ExoMars Trace Gas Orbiter. Since April 2018, when the nominal science mission began, it has been measuring the constituents of the Martian atmosphere. NOMAD contains three separate spectrometers, two of which operate in the infrared: the Solar Occultation (SO) channel makes only solar occultation observations, and therefore has the best resolving power ($\sim 20,000$) and a wider spectral region covering 2.2–4.3 μm . The Limb, Nadir and Occultation (LNO) channel covers the 2.2–3.8 μm spectral region and can operate in limb, nadir or solar occultation pointing modes. The Ultraviolet–Visible (UVIS) channel operates in the UV–visible region, from 200 to 650 nm, and can measure in limb, nadir or solar occultation modes like LNO.

The LNO channel has a lower resolving power ($\sim 10,000$) than the SO channel, but is still typically an order of magnitude better than previous instruments orbiting Mars. The channel primarily operates in nadir-viewing mode, pointing directly down to the surface to measure the narrow atmospheric molecular absorption lines, clouds and surface features in the reflected sunlight. From the depth and position of the observed atmospheric absorption lines, the constituents of the Martian atmosphere and their column densities can be derived, leading to new insights into the processes that govern their distribution and transport. Surface properties can also be derived from nadir observations by observing the shape of the spectral continuum.

Many calibration measurements were made prior to launch, on the voyage to Mars, and continue to be made in-flight during the science phase of the mission. This work, part 2, addresses the aspects of the LNO channel calibration that are not covered elsewhere, namely: the LNO ground calibration setup, the LNO occultation and nadir boresight pointing vectors, LNO detector characterisation and nadir/limb illumination pattern, instrument temperature effects, and finally the radiometric calibration of the LNO channel. An accompanying paper, part 1 (Thomas et al., 2021, this issue), addresses similar aspects for SO, the other infrared channel in NOMAD. A further accompanying paper (Cruz-Mermy et al., 2021, this issue) investigated the LNO radiometric calibration in more detail, approaching the work from a theoretical perspective. The two calibrations agree with each other to within 3%, validating each calibration method.

* Corresponding author.

E-mail address: ian.thomas@aeronomie.be (I.R. Thomas).

<https://doi.org/10.1016/j.pss.2021.105410>

Received 13 July 2021; Received in revised form 20 December 2021; Accepted 21 December 2021

Available online 28 December 2021

0032-0633/© 2022 The Authors. Published by Elsevier Ltd. This is an open access article under the CC BY license (<http://creativecommons.org/licenses/by/4.0/>).

1. Introduction

NOMAD (Nadir and Occultation for MArS Discovery) is one of four instruments on board the ExoMars Trace Gas Orbiter that has been observing the Martian atmosphere across a wide spectral range spanning the UV and IR since April 2018. It consists of 3 independently operated channels: SO (solar occultation), LNO (limb, nadir and occultation) and UVIS (ultraviolet and visible spectrometer) (Neefs et al., 2015; Patel et al., 2017). As is suggested by the name, the LNO channel can operate in nadir, limb and solar occultation mode.

The LNO channel can, if operating in occultation mode, detect the same trace gases as the SO channel, namely CO₂, CO, H₂O (incl. HDO), HCl and isotopologues (Aoki et al., 2019; Korablev et al., 2021; Liuzzi et al., 2020; Smith et al., 2021; Vandaele et al., 2019) although, as the channel is principally designed to operate in nadir mode, the resolving power is approximately 10,000, around half that of the SO channel (Liuzzi et al., 2019; Thomas et al., 2016).

In nadir mode, the channel principally measures column abundances of CO, H₂O, CO₂, clouds and surface features such as ice, and investigations are underway to determine if HDO can be detected and to calculate the upper limit for any CH₄ detection in nadir-viewing mode. The SNR in nadir mode for a single spectrum is around 10, but this can vary depending on the observing geometry and diffraction order; much less than in occultation mode due to the difference in signal level between observing reflected radiation and looking directly at the Sun (Thomas et al., 2016). With a high spectral resolution of around $\sim 0.3 \text{ cm}^{-1}$ (Liuzzi et al., 2019), the strongest Martian gas absorption lines can be measured in nadir mode. The global and local time coverage is much better than the SO channel (which is mainly limited to high latitude observations and regions along the terminator), which also means that the co-incident spectra can be averaged to increase SNR if required. NOMAD LNO continues to monitor the major seasonal cycles on Mars, extending existing datasets made by successive space missions in the past decades (e.g. Smith et al., 2021). Global datasets of H₂O and CO will be invaluable to monitoring changes in the atmosphere of Mars (Vandaele et al., 2015).

2. NOMAD LNO channel

An image of NOMAD is shown in Fig. 1. The LNO channel is based on the SO channel (Neefs et al., 2015), although with several important modifications: the entrance optics contains a flip mirror allowing both nadir and occultation pointing modes; the slit is longer and double the width, i.e. the equivalent of 150×4 pixels, reducing the spectral resolution but increasing the Instantaneous Field of View (IFOV) to 150×4 arcminutes; and the spectral range of the channel is reduced to 2.2–3.8 μm . This reduction is important, as the majority of the noise originates from the thermal background of the instrument itself, and so the thermal

noise is reduced by a factor of approximately two by blocking the 3.8–4.3 μm radiation from reaching the detector (Thomas et al., 2016).

The LNO channel is comprised of: entrance optics; an acousto-optic tuneable passband filter (AOTF); a spectrometer section, consisting of a slit and echelle diffraction grating spectrometer; and a cryocooled infrared detector array. As for SO, the AOTF acts as a passband filter, selecting the spectral interval that can pass into the spectrometer section and onto the detector. The bandwidth of this filter corresponds approximately to the Free Spectral Range (FSR) of the echelle spectrometer section, to maximise throughput and minimise out-of-band radiation from outside the desired diffraction order. The AOTF is driven by a radio frequency input, the frequency of which must be defined for each diffraction order so that the AOTF passband is centred on the desired diffraction order. The instrument can measure any one of around 100 diffraction orders, from ~ 110 to 210 and can switch from one order to another quasi-instantaneously. The Sofradir HgCdTe MARS-MW detector in the LNO channel contains 320 columns (spectral direction) and 256 rows (spatial direction) of pixels that are cooled to 85K during observations. Only 144 of the 256 spatial pixels are illuminated during a nadir observation, so many of the pixels at the top and bottom of the detector are never used.

The LNO flip mirror can be placed in one of two positions. When in nadir position, the channel field of view (FOV) is deflected “downwards”, which in normal operations is towards the centre of Mars, however the TGO satellite can slew so that the channel is instead directed towards the limb or off-nadir. When in occultation position, the mirror is no longer in the optical path and the FOV points in the same direction as the SO and UVIS occultation channels. This allows the LNO channel to observe solar occultations (in place of SO) and to run solar calibration and limb observations. Due to the sensitivity of the other instruments on TGO, the channel can never be pointed at the Sun with the flip mirror in the nadir position. More technical details on the NOMAD instrument, and in particular the infrared channels, can be found elsewhere (Neefs et al., 2015).

3. Measurement parameters

The wavelength of the AOTF passband can be changed quasi-instantaneously, and so any diffraction order can be measured within the spectral range of the channel. In nadir mode, SNR considerations typically limit an LNO nadir observation to 1–6 diffraction orders measured every 15 s. This 15 s period is known as the rhythm: the rhythm period is divided by the number of diffraction orders measured; for example, if 3 orders are measured then each is allocated 5 s of measurement time (Table 1). The channel cycles through the chosen orders within this period, then returns to the first diffraction in the next rhythm period, etc., until the observation ends. A better SNR is achieved by measuring fewer orders, so that a longer measurement time is allocated to each order - however this means that fewer gas species can be measured together on that orbit - and so two or three orders are typically measured as a compromise. For surface ice/cloud detections, it is more important to have broader spectral coverage (hence more diffraction orders) whilst resolving individual gas lines is not necessary, hence four or six order measurements are more common.

Detector background acquisitions, where the AOTF is switched off, are made immediately before each Mars acquisition, using the same observation parameters. An unpowered AOTF is opaque, and so the only radiation reaching the detector comes from the thermal background of the channel itself. Each Mars acquisition (consisting of the signal from Mars + instrument thermal background) is then subtracted from each background acquisition (consisting of instrument thermal background only) to leave the Mars nadir spectrum, which is then transmitted to Earth.

This background acquisition method has the advantage that the background is accurately removed, however the disadvantages are that half of the observation time is effectively lost, and the raw background

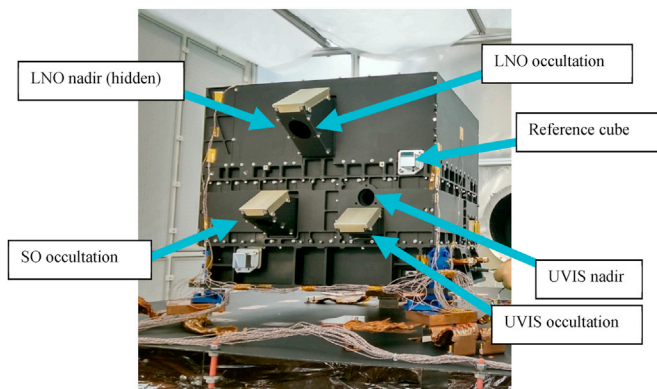


Fig. 1. A photo of NOMAD, taken during ground calibration. The channel apertures and main reference cube are labelled.

signal is lost (as only the subtracted values are transmitted back to Earth). For nadir observations, background subtraction is always performed onboard the spacecraft, otherwise the Martian signal would be significantly degraded by the data reduction methods employed onboard to compress the spectra for transmission to Earth; whereas solar occultation measurements can be made with background-subtraction on or off, see part 1 (Thomas et al., 2021, this issue).

For transmission to Earth, the detector rows are binned depending on the number of diffraction orders measured - LNO can return 24 lines of spectra per rhythm period, therefore if only one diffraction order is chosen then 24 lines of spectra are returned, each corresponding to a different region on the detector and a different IFOV on the planet's surface. Due to the limited SNR, the different detector bins measured simultaneously in nadir mode are summed together; in occultation mode the bins are analysed separately. In solar occultation mode, the LNO channel operates in the same way as SO (Thomas et al., 2021, this issue). Solar occultation observations are self-calibrating, and therefore did not require on-ground radiometric calibration, except to define the illuminated detector rows, non-saturation integration time, and AOTF driving frequencies for each diffraction order. Therefore much of the ground calibration campaign was dedicated to the LNO nadir channel, which requires other means of radiometric calibration.

In addition to scientific measurements of specific diffraction orders, NOMAD has a calibration mode, known as "stepping" measurements, where a measurement parameter (such as integration time, AOTF frequency, diffraction order, detector row, etc.) is incremented continuously from a starting value for a set number of steps. This is particularly important for calibration observations, allowing the channel to "step" through the entire spectral range of NOMAD or measure at many different integration times in a single observation.

Due to the complex nature of the instrument, effectively containing three separate spectrometers that operate in multiple observation modes, the complete calibration of the instrument is divided into several separate studies: for LNO AOTF and spectral calibration, more details are presented elsewhere (Liuzzi et al., 2019). A companion paper (Thomas et al., 2021, this issue) deals with SO calibration, and a further companion paper (Cruz-Mermy et al., 2021, this issue) contains a complementary LNO radiometric calibration.

4. Calibration

4.1. LNO calibration objectives

The main instrument calibration objectives are detailed in Table 2. In occultation mode, radiometric calibration is not necessary - as the Sun is observed unobstructed at the start or end of every measurement - though spectral calibration and detector characterisation are still required. In nadir mode, no such reference measurement exists, and so a full calibration is essential.

Table 1

Examples of detector pixel binning regimes for various observation types (solar occultation; nadir; special surface observations; and calibration). Note that the observation time includes detector readout time, data processing time, and dark measurements.

Sampling Rhythm (seconds)	No. of diffraction orders per rhythm	Observation time per diffraction order (including dark)	No. of lines per rhythm	No. of lines per diffraction order	No. of detector lines used	Pixel binning required
1 (occultation)	6	1/6th s	24	4	16	4
15 (nadir)	6	2.5 s	24	4	144	24
15 (nadir)	4	3.75 s	24	6	144	24
15 (nadir)	3	5 s	24	8	144	18
15 (nadir)	2	7.5 s	24	12	144	12
15 (nadir)	1	15 s	24	24	144	6
15 (surface)	4	3.75 s	24	6	72	12
1 (calibration)	1	1 s	24	24	24	none

4.2. Ground calibration

NOMAD was mounted in a thermal vacuum chamber at the Centre Spatial de Liege in Liege, Belgium for the entire ground calibration campaign. The chamber was equipped with a flange containing three window ports at the same height as the LNO FOV, the UVIS FOV, and the NOMAD reference cube. The LNO port contained a sapphire window, transparent in the infrared, while the UVIS and reference cube windows were made of quartz to be transparent in the visible spectral region. Inside the chamber, NOMAD was surrounded by a temperature-controlled shroud, with small cut-outs at the same heights as the three windows, so that the LNO and UVIS channel FOVs passed through the windows and the reference cube could be viewed from outside the chamber.

The SO and LNO channel calibration setup (Fig. 2) was mounted on a gantry outside the chamber, directly attached to the outside of the chamber flange containing the port windows. It was not possible to make the calibration enclosure completely airtight, and so a nitrogen line fed a continual overpressure of nitrogen gas into the enclosure to ensure that minimal atmospheric air was present. With the chamber closed and evacuated to a pressure $<10^{-5}$ mbar, and the nitrogen overpressure switched on, terrestrial atmospheric absorption lines were successfully suppressed.

The setup (Figs. 2 and 3) contained equipment for calibration of both the infrared and ultra-violet channels; however only the infrared channel equipment will be described here. For LNO, the following equipment was used:

- Spirit level, visible laser and several 2 mm apertures for alignment of the setup.
- HGH Infrared Systems DCN1000N 100 × 100 mm blackbody, on a motorised linear translation stage. The blackbody has emissivity 0.98 ± 0.02 and uniformity of 0.1C across the blackbody area. This is within the required uniformity.
- Five Specac 10 cm pass gas cells, containing 21 mbar CH₄, 264 mbar CO, 93 mbar CO₂, 26 mbar C₂H₂ or 1000 mbar N₂ gas, on a motorised rotation stage. A sixth space was available on the rotation stage (Fig. 2), without a gas cell, so that measurements could be made of the Globar without a gas cell present.
- LOT-Oriel 6363IR Infrared Globar and housing, with radiance peak at 3 μm, used as a broadband illumination source behind the gas cells. No specifications were required except that the source must be stable to <5% over the duration of a spectrum acquisition (1–15 s), and that ideally the source's radiance curve should be spectrally flat across each diffraction order, so gas cell absorption bands can be easily distinguished. The Globar source was compliant with these requirements.

The blackbody was sufficiently large that it filled the entire field of view (FOV) of LNO, providing a uniform temperature target for radiometric calibration tests. The blackbody signal was low at shorter

Table 2

An overview of the calibrations performed and the observations required to achieve them.

Calibration type	Observation description	Justification/Precision Requirement
Boresight pointing direction	LNO occultation boresight: in-flight solar line scan	The field of view must point towards the centre of the solar disk during a solar occultation observation. Precision: <2 arcminutes to achieve good solar signal.
	LNO nadir boresight: in-flight Mars limb scan	To know where on the surface LNO was observing. Precision: no requirement, but less than 1/10 the FOV width (i.e. < 15 arcminutes) would be ideal.
Slit position and relative illumination of detector rows	In-flight solar line scan	The detector rows with the highest signal have the best SNR. Precision: Cut-off of illuminated region known to nearest pixel.
Detector column slant	Gas cell observations during ground calibration	When detector rows are binned, the effective spectral resolution is reduced if absorption lines are spread across different pixels. Precision: no requirement, but a slant reduces the observed spectral resolving power.
Bad pixel detection	Integration time stepping observation when viewing blackbody (on ground) or dark sky (in-flight)	Bad/anomalous pixels give incorrect transmittance values, and so should not be used in retrievals or further analysis. Precision: all bad pixels must be known. Blackbody emissivity uniformity >90% ideally for bad pixel detection.
Detector saturation level	LNO occultation: In-flight integration time stepping observation when viewing Sun	A saturated detector gives incorrect transmittance spectra, and so this must be avoided. Precision: nearest millisecond.
	LNO nadir: Integration time stepping observation when viewing blackbody (on ground) or dark sky (in-flight).	A saturated detector gives incorrect transmittance spectra, and so this must be avoided. Precision: nearest 100 ms.
AOTF/grating spectral calibration	The first analysis used gas cell observations in ground campaign (setup described here). Further analysis used in-flight solar observations, as detailed elsewhere (Liuzzi et al., 2019).	The ground calibration setup was needed to calculate a first version of the calibration (e.g. to define the diffraction orders), to be refined later from in-flight observations. Precision: gas cell lines known to 1/10th of spectral resolution ($\sim < 0.025 \text{ cm}^{-1}$) ideally
Diffraction grating temperature effects	Gas cell measurements (ground calibration) and solar line spectra (in-flight)	As the temperature of the channel changes, the position of absorption lines on the detector moves: a correction is

Table 2 (continued)

Calibration type	Observation description	Justification/Precision Requirement
Radiometric calibration (to transmittance for LNO occultation; to reflectance factor for LNO nadir)	LNO occultation: the counts-to-transmittance conversion method is detailed elsewhere (Trompet et al., 2016).	required to shift the pixel-to-wavenumber relation to account for this. Precision: uncertainty <1 pixel ideally Spectra must be converted to transmittance for further analysis e.g. retrievals. Precision: SNR >1000 for occultation spectra, typically 2000–3000 in the centre of the detector.
	LNO nadir: in-flight solar observations	Spectra must be converted to reflectance factor for further analysis e.g. retrievals. Precision: Systematic errors should be <10%. SNR will be depend on observation parameters; expected to be ~15–20 in good conditions.

wavelengths, and so the Global was used to illuminate the gas cells: it operates at 800–1000 K, easily sufficient to operate across the full spectral range of the NOMAD SO and LNO channels. The Global hot element did not fill the entire FOV, just ~100 of the 144 detector rows, but this is not critical for spectral calibration observations. Motorised linear stages were used so that the gas cell and blackbody sources could be interchanged within the enclosure without needing to open it up each time, preserving the Nitrogen overpressure. The Global was switched on/off manually, but the blackbody temperature and both motorised stages were controlled by computer, with information written to a log file each time a change was made, to assist in subsequent analysis.

Optical alignment was achieved using the laser and 2 mm apertures. First, the optical baseplate was fixed horizontally using a spirit level, as was also done for NOMAD. Then the apertures were mounted parallel to the baseplate, and the laser orientated so that the beam passed directly through the centre of both apertures. An additional mirror, used purely for alignment, was also mounted parallel to the baseplate axis, such that the beam bounced directly back through both apertures and back onto the laser – which ensured that the laser was mounted parallel to the baseplate in a known position. With the laser mounted, the baseplate was then aligned to NOMAD when the laser beam could pass through the apertures, hit the centre of the reference cube, and back again through the two apertures onto the laser. The adjustable legs on the baseplate were locked in place and all the calibration equipment was then secured to the baseplate. An aperture attached to the linear translation stage was used to check the position of the laser beam with respect to the position of the stage, to ensure that the motorised stage's zero position was correct.

4.3. In-flight calibration

The main types of in-flight calibration observations are solar FOV scans, Mars limb scans, fixed solar pointing, and dark sky observations. During solar FOV scans, the spacecraft is slewed such that the LNO occultation channel FOV passes in and out of the solar disk. A similar method is used for the limb scans, where the spacecraft is slewed so that the LNO nadir field of view crosses the illuminated limb of the planet, as the nadir-pointing face of the spacecraft cannot be pointed directly at the Sun. For solar observations, the spacecraft points the FOV continuously towards the centre of the Sun; similarly, for the dark sky observations the FOV is pointing in a fixed direction away from the Sun or Mars. More details of each in-flight calibration observation are given in each part of

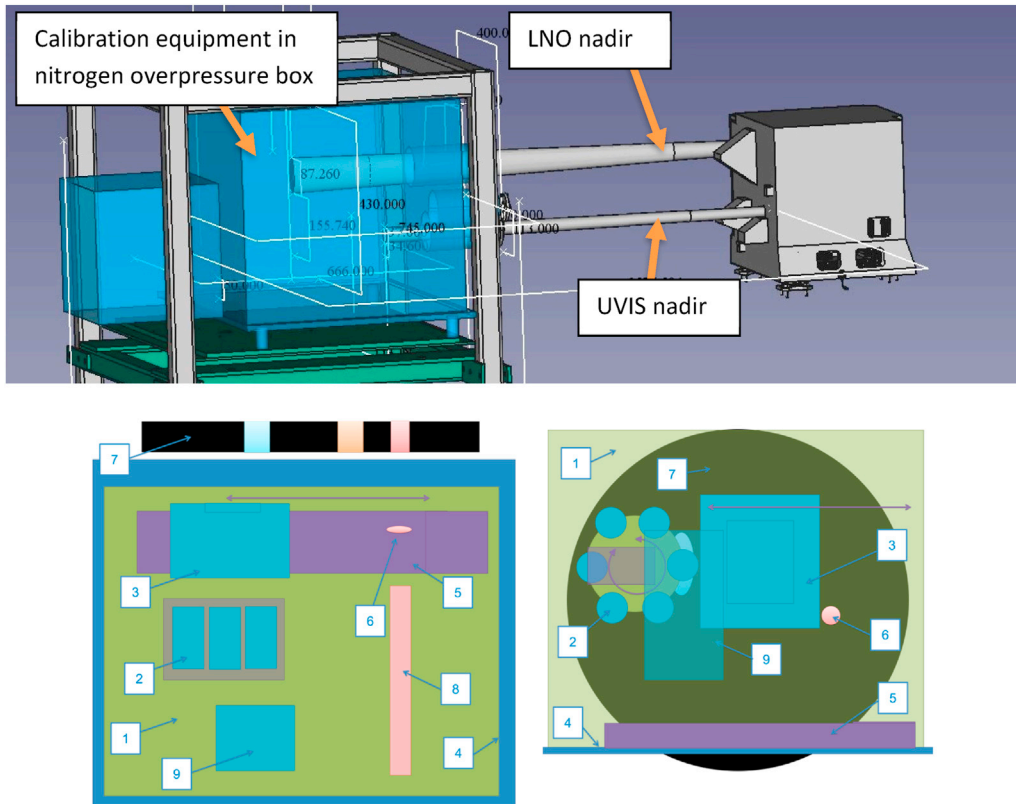


Fig. 2. Top: A schematic showing the position of NOMAD with respect to the LNO calibration setup (blue). The vacuum chamber and instrument support structure is not shown here for clarity. Bottom: Plan view (left) and back view (right) of the calibration setup. The numbers correspond to the following parts: 1) Enclosure, made of opaque black Plexiglas; 2) IR gas cells and rotation stage; 3) Blackbody mounted on linear stage; 4) Optical baseplate; 5) Motorised linear translation stage; 6) Pin hole for translation stage alignment; 7) Vacuum chamber window with LNO (blue), UVIS (orange) and Reference cube (red) windows; 8) Laser for optical alignment; 9) Globar hot source.

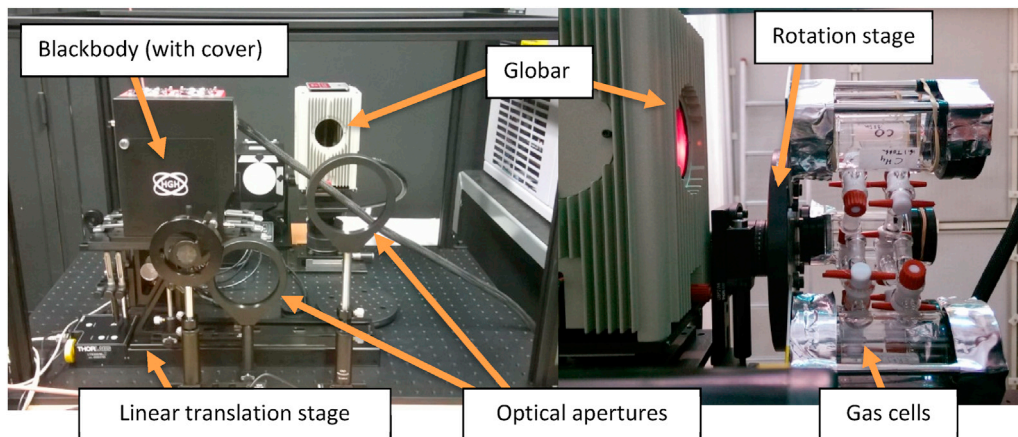


Fig. 3. Left: a photo of the calibration setup, with optical mounts in place to represent the thermal vacuum chamber windows, prior to mounting of the gas cells. The calibration equipment for UVIS can be seen here, though it is beyond the scope of this work. Right: the infrared gas cells, placed in front of the hot Globar source. The outer framework holds the enclosure in place.

the results section.

5. Results

5.1. Slit position and relative illumination

The slit position and relative illumination on the LNO detector were determined in the same way as for the SO channel (Thomas et al., 2021, this issue). The main difference is that the LNO slit is much longer, and hence many more detector rows are illuminated. The detector contains 256 rows of pixels, in nadir mode only 144 rows are read out, and therefore the rows with the best illumination must be selected to optimise the nadir observations. Fig. 4 shows how the signal on the centre

detector row changes as the FOV moves across the solar disk during a solar line scan. As described in the measurement parameters section, during a single frame acquisition only 24 detector rows can be read out, and therefore to cover the whole detector a "window stepping" measurement is performed. In this mode, detector rows are read out sequentially, e.g. rows 1–24, 25–48, etc. until all 256 rows have been measured and the acquisition starts again from row 1. This builds up a picture of the vertical illumination pattern on the detector, so that the width and centre of the illuminated region can be determined; the results of this are shown in Fig. 5.

Note also that the detector rows are not uniformly illuminated; the relative signal strength of the highest and lowest illuminated rows is around 75% of the centre row (Fig. 5). The illumination pattern was

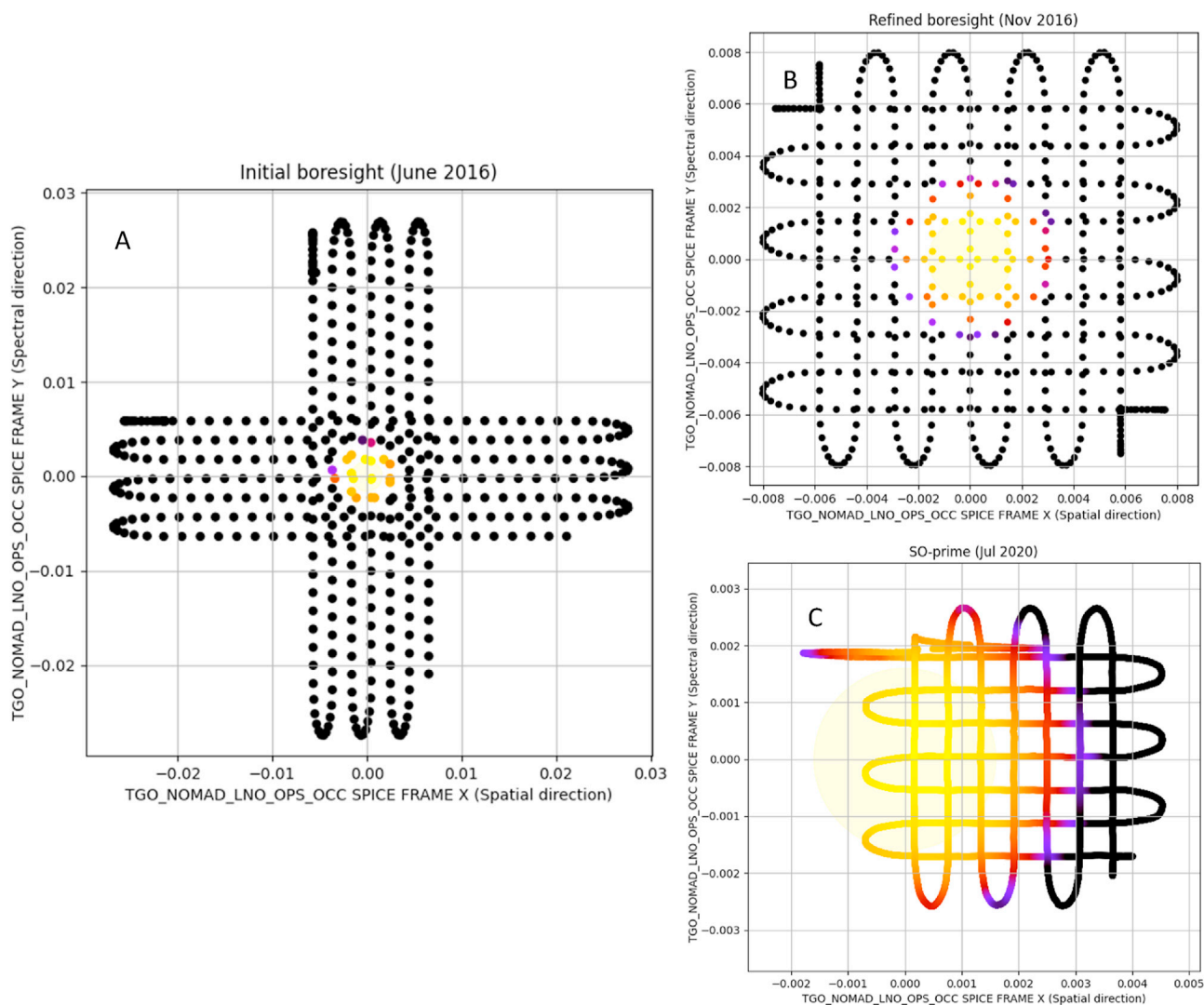


Fig. 4. LNO channel solar line scans, where the spacecraft is slewed so that the FOV passes through the solar disk in two orthogonal directions, X and Y. (A) For the earliest scans, a larger grid is used as the LNO slit is longer, therefore the spacecraft needs larger slews to illuminate all detector rows. Follow up observations (B) used a smaller grid; then the same grid as SO (C). The FOV scan in (C) was centred using the SO boresight, hence the Sun appears to be misaligned; however the Sun centre is still located at (0.0003, 0.0001) in the LNO occultation reference frame. The X axis represents the detector spatial direction; the Y axis represents the detector spectral direction, and the units of each represent the vector coordinates in the X,Y plane (i.e. 0 is parallel and 1 is perpendicular). The colour represents the signal on the centre row of the detector, from black (space) to yellow (solar centre); the boresight pointing vector is calculated by comparing the position of the Sun measured by LNO to the pointing direction of TGO throughout the line scans.

found to be centred on row 152 for the LNO channel, and so a nominal nadir observation of 144 rows uses detector rows 80–224.

5.2. Line of sight calibration

5.2.1. LNO occultation channel

Now that the detector row at the centre of illuminated region is known, the boresight pointing vector (the direction of the field of view centre with respect to the spacecraft) can be calculated for the FOV centre by analysing how the illumination pattern changes as the FOV is slewed around the solar disk. This is essential for LNO solar occultation observations, where the field of view must remain as fixed as possible on the Sun during the observation. As for the SO channel (Thomas et al., 2021, this issue), the final boresight vector was refined from multiple solar line scans, starting from the alignment calculated during assembly. After launch, the FOV of each channel was raster-scanned around the Sun in two perpendicular dimensions (Fig. 4), first with a large scan grid (A) to ensure the Sun was observed, followed by progressively smaller grids (B

and C). The LNO FOV scans are run less regularly than SO (typically every 15 months), as the channel is primarily used for nadir and limb observations rather than solar occultations.

For solar occultations an accuracy of <2 arcminutes is required. The calculated solar centre is located at coordinates (0.0003, 0.0001) in Fig. 4 (C), which corresponds to a deviation of 1.0 and 0.3 arcminutes in the X and Y axes from the current boresight i.e. around half of the required accuracy.

5.2.2. LNO nadir channel

For the LNO nadir channel, the Sun cannot be used as the source, as the spacecraft is forbidden from pointing the nadir face towards the Sun. Instead, the FOV was scanned several times across the sunlit limb of Mars in two dimensions. With background subtraction enabled, a signal of zero \pm noise is returned for dark space observations (Fig. 6: sequences 1 and 6). Then as the spacecraft is slewed, the signal peaks as the sunlit planet enters the FOV (sequences 2 and 6) and similarly decreases when passing back into dark space (sequence 4). As was done for the solar

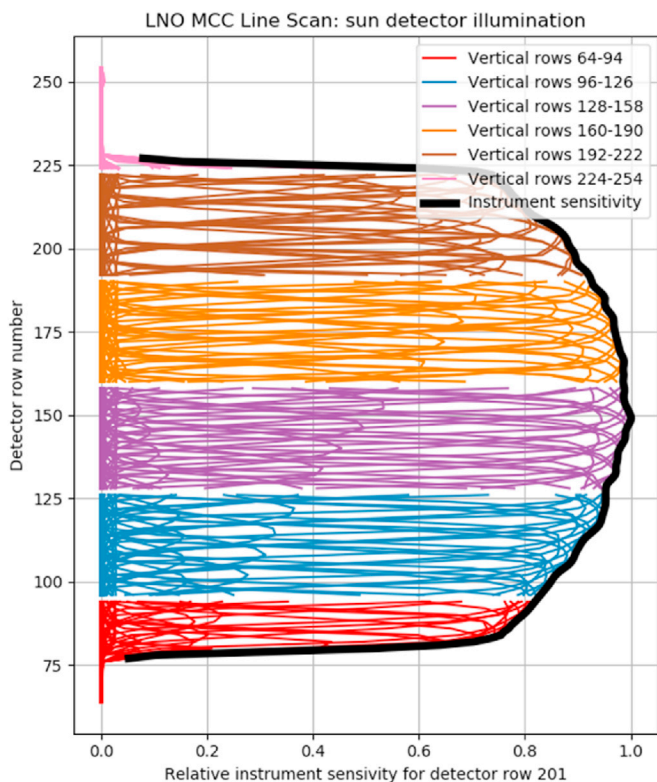


Fig. 5. LNO detector row illumination patterns, as measured during an in-flight solar line scan calibration. During a solar line scan, the spacecraft is slewed so that the FOV of each channel passes in and out of the Sun, while spectra are recorded by every pixel individually using the same AOTF frequency. A vertical column on the detector is chosen (here for spectral pixel 230) and the signal for each pixel is plotted. The region of the detector illuminated by radiation entering NOMAD is given by the full-width half-maximum, and the central detector row is defined as the centre of the illumination pattern. Gaps are observed as only 24 detector rows are read out at any one time, and so separate detector acquisitions are made to check the illumination on all rows.

occultation channel, the detector peak signal is correlated to the spacecraft pointing direction to determine the boresight vector. Fig. 6 panels B + D show the variation in signal versus time in the two scan directions, where the sunlit limb of Mars is perpendicular (A + B) and parallel (C + D) to the slit. The LNO FOV has an angular extent of 144×4 arcminutes, which for these observations was split into 12 bins of 12×4 arcminutes each. The limb scans were taken prior to aerobraking when TGO was $\sim 25,000\text{--}30,000$ km from Mars, hence the size on the limb of one bin was around 100×30 km. This meant that the size of the atmospheric limb of Mars was smaller than the FOV size, and the limb signal lower than that reflected off the surface, therefore scattering from the sunlit limb did not affect the boresight determination.

In Fig. 6 panel B, there are 60 s between each vertical line in sequences 2, 4, and 6, which corresponds to the time at which each of the plotted bins crosses the sunlit limb. For clarity, only four bins (2nd, 5th, 8th and 11th) so this equates to a 20-s time difference between adjacent bins. As the FOV was slewed at 0.6 arcminutes per second, each bin FOV is therefore $20 \times 0.6 = 12$ arcminutes long, exactly as expected.

There were 7.5 s between each frame acquisition, so when moving at 0.6 arcminutes/s the boresight is likely to be accurate to approximately 5 arcminutes in both directions. This is ~ 1.25 times the width of the shortest edge of the IFOV and $\sim 1/40$ th of the width of the longest edge of the IFOV. Further limb scan observations cannot be made post-aerobraking, so there is no possibility of repeating the measurement to check, however there may be future opportunities to check the pointing, for example with observations of Phobos or Deimos.

5.3. Detector smile/slant

Ideally, the centre of an absorption line would be present on the same spectral pixel for all detector rows. Spectrometer optics cause small distortions from the ideal case, and an absorption line may be slightly shifted with respect to the rows above and below. This effect is known as the detector smile, as often the peak of the shift appears in the centre of the detector causing it to look like a smile or frown.

Such shifts are typically sub-pixel, and so it is not sufficient to simply define the smile based on the pixel containing the smallest value; instead a Gaussian fit needs to be made to the absorption to determine the exact pixel position (in fractions of a pixel) on which the centre of the absorption minimum lies. To achieve the best fit possible, it is necessary to use high SNR observations which cover a large number of detector rows. The SNR of Mars nadir and blackbody observations are too low, giving poorly constrained fits, and solar occultations and calibrations have high signal but only cover ~ 20 rows i.e. the width of the solar disk. The gas cells illuminated by the Globar, as measured during ground calibration, provide a good trade-off between SNR (the Globar peaks at $3 \mu\text{m}$) and detector row coverage (almost 100 detector rows are illuminated). Using ground calibration data also allows us to check for instrument temperature effects, as measurements were made at five temperature setpoints.

Examples of the detector smile are shown in Fig. 7, for the same absorption at different instrument temperatures (horizontally, A-B and C-D) and for different diffraction orders at the same temperature (vertically, A-C and B-D). All the strongest gas cell molecular absorptions measured during the ground calibration campaign have a similar shape, with a minimum spectral pixel around row 152 (i.e. the centre of the illuminated region). In total, the observed smile is around 0.5 pixels in extent, however the Globar does not illuminate the entire field of view, and hence a smile of around 1.25 pixels is a more realistic estimate over the entire illuminated detector region (i.e. rows 80 to 224). As the nadir data is vertically summed to improve SNR, producing a single spectrum per detector frame, the smile measured here will cause an absorption band to spread over an additional 1.25 pixels, increasing the width of the instrument line shape. Differences between the detector smile when the instrument is cold and hot are small, and negligible when considering that the SNR of the LNO nadir channel is around 10.

5.4. Bad pixels

The LNO detector contains bad pixels, which are those that give a non-linear radiance-to-ADU response to incoming photons. Some pixels behave non-uniformly to changes in intensity of incoming radiation, and some give the same value irrespective of the level of incident radiation. Such pixels need to be identified and removed before the spectra can be correctly analysed.

Integration time stepping observations, where each pixel is read out individually as the integration time is increased incrementally from $1 \mu\text{s}$ (the smallest readout time possible) to a maximum value of 1.7 s were used for this purpose, when the instrument was viewing a uniform source i.e. observations of the blackbody during ground calibration and of dark sky during in-flight calibrations. The total number of photons hitting the detector is proportional to the integration time, as the majority of the radiation hitting the detector is thermal background from the instrument itself, and so the radiance of the source is not important, so long as it is uniform.

More than 99.9% of all LNO pixels show a similar linear relationship between ADU counts and radiance; the other 0.1% have large deviations from the linear ideal, and are therefore designated as bad pixels. These pixels stand out on a chi-squared goodness-of-fit plot such as that in Fig. 8; here any pixel with a chi-squared higher than 200,000 was considered to be a bad pixel. This value was chosen by trial-and-error, first by setting a high cut-off value of 500,000, locating the bad pixels, and removing them from LNO nadir spectra. Around 50 spectra from different observations were randomly selected for this, after which the

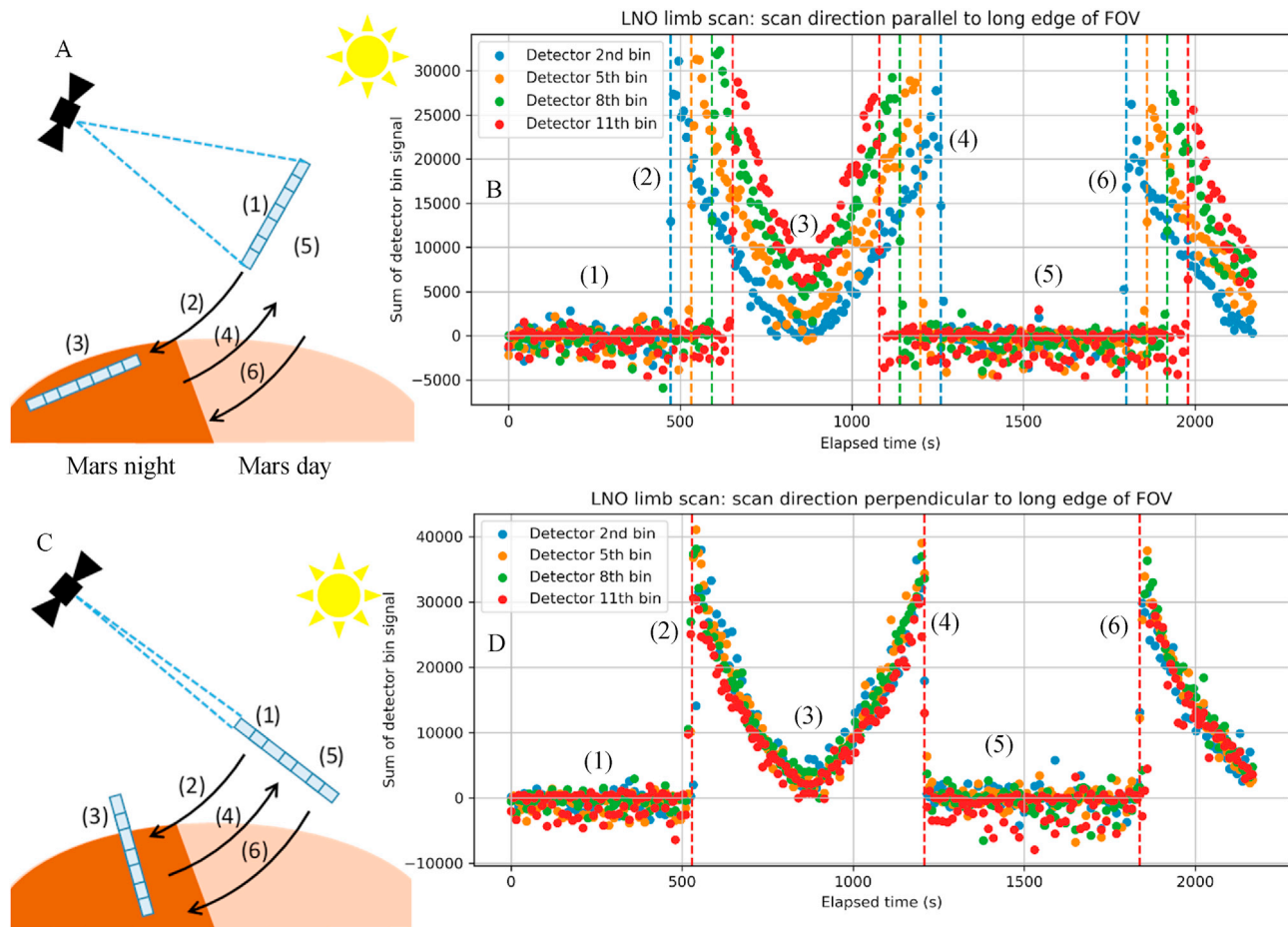


Fig. 6. LNO detector signal on four detector bins as the FOV is slewed across the sunlit limb of Mars. A + B: The scan direction is parallel to the long edge of the FOV (i.e. perpendicular to the Mars limb); B + D: The scan direction is perpendicular to the long edge of the FOV (i.e. parallel to the Mars limb). The observation sequence is as follows: (1) the signal on each bin is zero when viewing dark space; (2) the signal peaks as the sunlit limb enters the FOV of the bin; (3) the slew continues to the non-illuminated region of the planet and then reverses direction; (4) the signal peaks again as the FOV views the sunlit limb; (5) zero signal when viewing dark space; (6) the signal peaks as the sunlit limb enters the FOV. When slewing parallel to the long edge of the FOV, the bins hit the limb at different times (B); when slewing perpendicular, the bins hit the limb at the same time (D). The sunlit limb-crossing points, shown as vertical dashed lines, are analysed to determine the pointing vector of each bin and thus the entire FOV.

spectra were checked by eye for spikes due to bad pixels. The nadir spectra are binned, and the binning depends on the number of diffraction orders (Table 1; 7th column), so it is difficult to determine the location of bad pixels from the spectra themselves. If bad-pixels were observed in the randomly chosen spectra, the cut-off value was reduced by 100,000 and the analysis rerun. No noise spikes were observed in nadir spectra once the cut-off had been set to 200,000, therefore this value was chosen.

5.5. Detector saturation

For optimal performance, a good integration time must be chosen: if it is too small, the signal acquired by each pixel will be small and the resulting spectrum noisy; if the integration time is too large then the detector will saturate and the spectrum is lost. For LNO occultation measurements, the solar flux is the main source of radiation, therefore this was determined during in-flight calibration where the Sun was directly observed following the same method as for the SO channel (Thomas et al., 2021, this issue). The saturation time and maximum detector signal were first determined for one diffraction order, using an integration time stepping observation whilst pointing directly at the Sun. To determine the saturation for other diffraction orders, the Sun was then observed in all diffraction orders with a non-saturated integration time, to define the relative instrument sensitivity compared to the one diffraction order with a known saturation time. The results for the LNO

channel are shown here in Fig. 9. An integration time of 2.0 ms is a good choice to avoid saturation in any diffraction order when viewing the Sun.

For nadir observations, the detector saturation time is predominately determined by the instrument temperature, ranging from 1000 ms if the instrument is very cold (-15°C) down to 200 ms if the instrument is warm ($>15^{\circ}\text{C}$). The typical in-flight operating temperature is around -10 to $+10^{\circ}\text{C}$, and so a conservative integration time of around 200 ms is always used to ensure that no saturation occurs. Multiple accumulations are co-added onboard to maximise the total surface observation time, and so the actual nadir integration time chosen has a small effect on the signal recorded. In order to maximise the number of accumulations within each rhythm period, the integration time is tweaked slightly: 200 ms for 2 diffraction orders, 205 ms for 3, 195 ms for 4, and finally 220 ms for 6 diffraction orders measured within each rhythm period.

5.6. AOTF and spectral calibration

The AOTF is a passband filter which is used to select which diffraction order reaches the spectrometer section of the instrument and thus the detector. The wavenumber of the passband is selected by applying a radio-frequency to the crystal, and therefore the best AOTF frequency needs to be found for every diffraction order, so that the central wavenumber of the AOTF passband corresponds to the central wavenumber of the diffraction order being measured. This maximises the throughput,

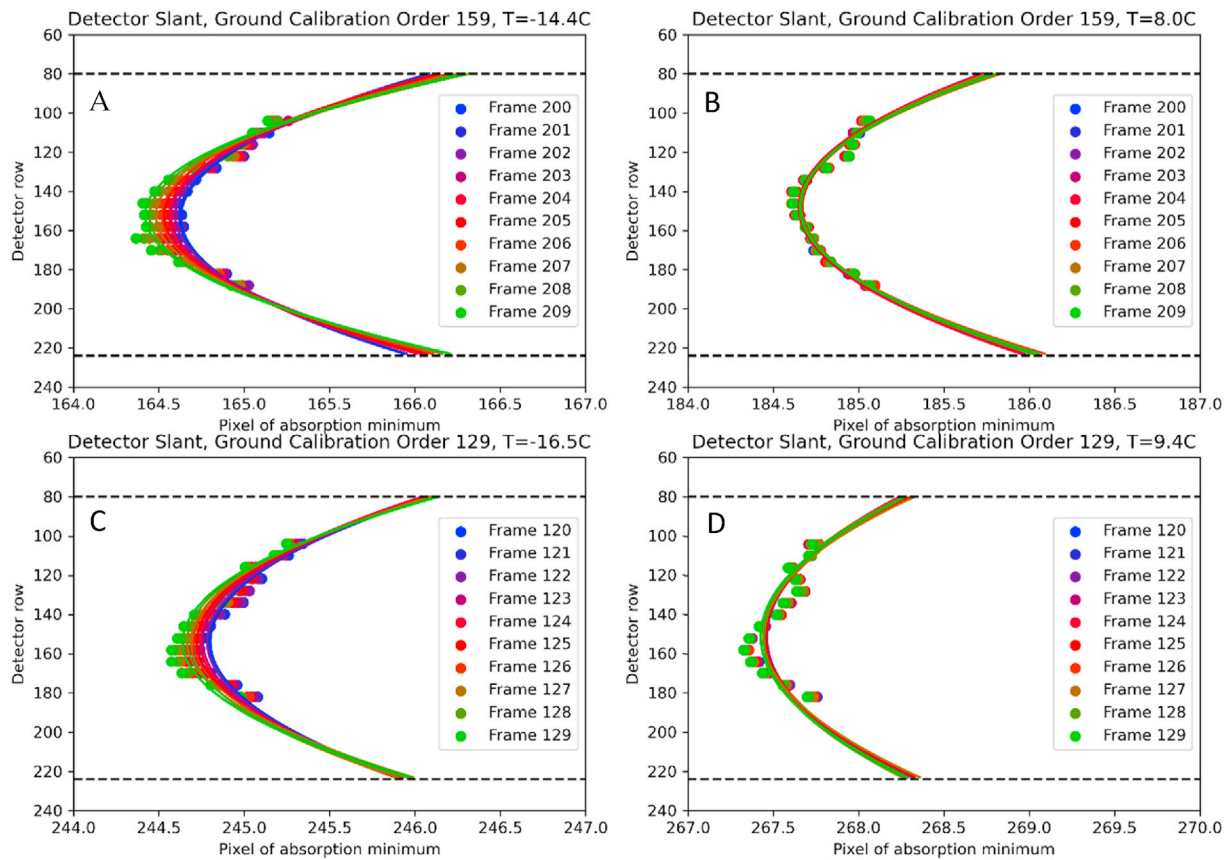


Fig. 7. LNO detector ‘smile’ as derived during ground calibration for different diffraction orders and instrument temperatures: (A) CO₂ gas cell, NOMAD cold; (B) CO₂ gas cell, NOMAD hot; (C) CH₄ gas cell, NOMAD cold; (D) CH₄ gas cell, NOMAD hot. The pixel position of an absorption line minimum is calculated by a Gaussian fit for each spectrum measured by each detector bin. Each detector frame is measured 10 times, and a small shift is observed in successive frames, likely due to the temperature of the instrument increasing slightly between each acquisition (the shift is bigger when the instrument is cold, as it heats up quicker). The pattern is repeatable for different orders, different positions on the detector, and different instrument temperatures, where the absorption minimum moves by around 0.5 pixels from row 152 (centre row) to rows 100 and 185. The horizontal lines indicate the extent of the detector readout during a nominal nadir observation: the Globar does not illuminate all the binned detector rows, and so quadratic fits (solid lines) extrapolate the slant across all nadir detector rows for each frame. This fit indicates that the smile covers ~1.25 pixels on average across the whole illuminated region.

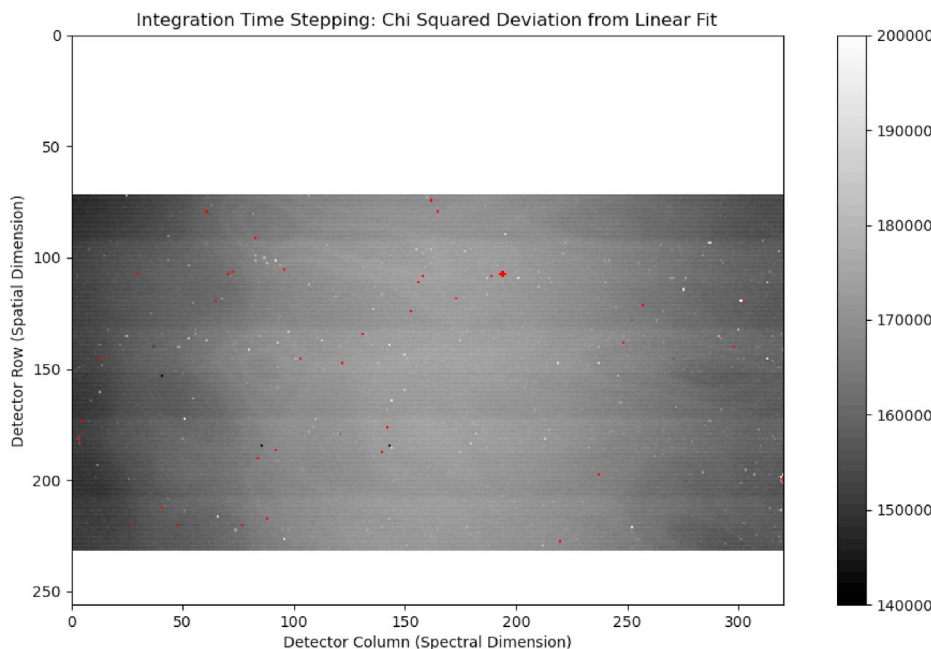


Fig. 8. LNO bad pixel map, prior to the start of the nominal science phase. Detector lines 72 to 232 were measured, where the colour indicates the chi squared deviation from a linear fit (white is less linear, black is more linear, red is very non-linear [off the colourbar chart i.e. > 200,000] or where the gradient is abnormal). The bad pixels stand out in red, while the detector manufacturing pattern is visible in the background values. The entire detector cannot be measured in a single observation, and therefore the image is made of multiple observations stitched together. The observations were made in groups of two, with a cool-down period between each group: this causes the horizontal stripes, as the linear fit is slightly different between observations where NOMAD is at a slightly different temperature, around 5 °C higher for the even-numbered stripes.

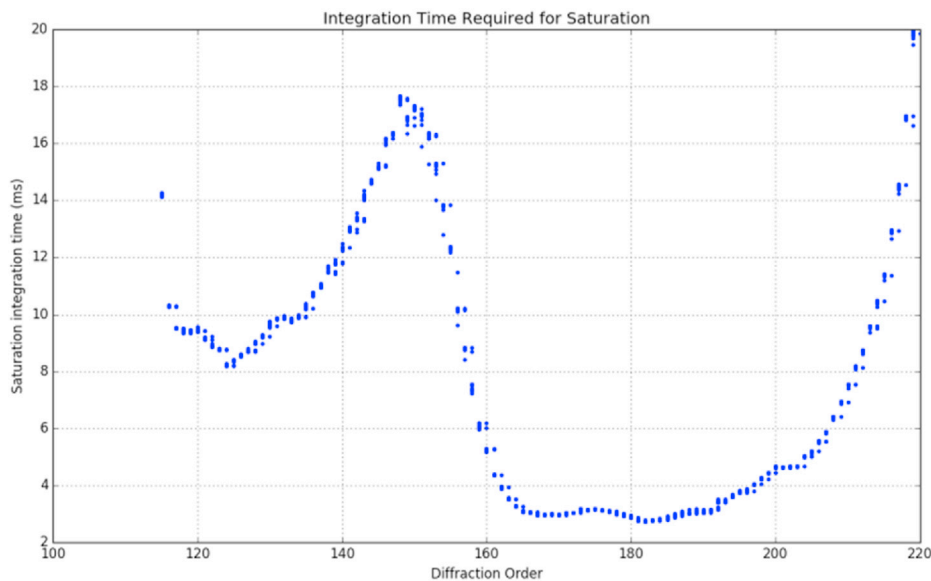


Fig. 9. LNO solar occultation saturation time. The shape is very similar to the SO channel, except that the increased slit width permits more radiation onto the detector, which subsequently saturates at a lower integration time.

and therefore the SNR, and reduces the presence of atmospheric lines from adjacent diffraction orders which can complicate the analysis.

For NOMAD to run calibration measurements, AOTF frequencies need to be uploaded to the instrument (along with information such as integration time, illuminated detector rows, etc.), which necessitates that the calibration is made in several steps. First, an approximate wavenumber-frequency relationship was found in the lab, before the AOTFs were integrated into the instrument, where a monochromator was used to shine specific wavelengths of light through the AOTF and onto a detector. This was done for multiple AOTF frequencies, to correlate the AOTF peak transmission wavelength with driver frequency. This approximate relationship was uploaded to the instrument, which was then refined during ground calibration. In the thermal vacuum chamber, the gas cells were measured and an improved set of AOTF frequencies corresponding to each diffraction order were then uploaded to the instrument. Once in flight, further measurements were made of the Sun, using the AOTF frequency calibration derived on the ground, and the AOTF shape, the

AOTF-frequency-to-central-wavenumber relation, AOTF-frequency-to-diffraction-order relation and diffraction grating parameters were then determined using in-flight data for the LNO channel (Liuzzi et al., 2019). The values measured on the ground were very similar to those measured in-flight: for example, for order 167 the optimum AOTF frequency measured on the ground was 24,025 kHz; the final in-flight value was 24,026 kHz, just 1 kHz different. As 150 kHz represents the difference between adjacent diffraction orders, a 1 kHz error is <1% of a diffraction order and equates to just 2 pixels on the detector.

5.6.1. Temperature dependency of spectral calibration

The in-flight diffraction order stepping observations are ideal for calibrating and checking the instrument, but in-flight the thermal environment and hence instrument temperature cannot be controlled (unlike in the thermal vacuum chamber). Therefore, to understand temperature-related effects, the ground calibration data are essential. In particular, the pixel-to-wavenumber relation is highly dependent on temperature, as the

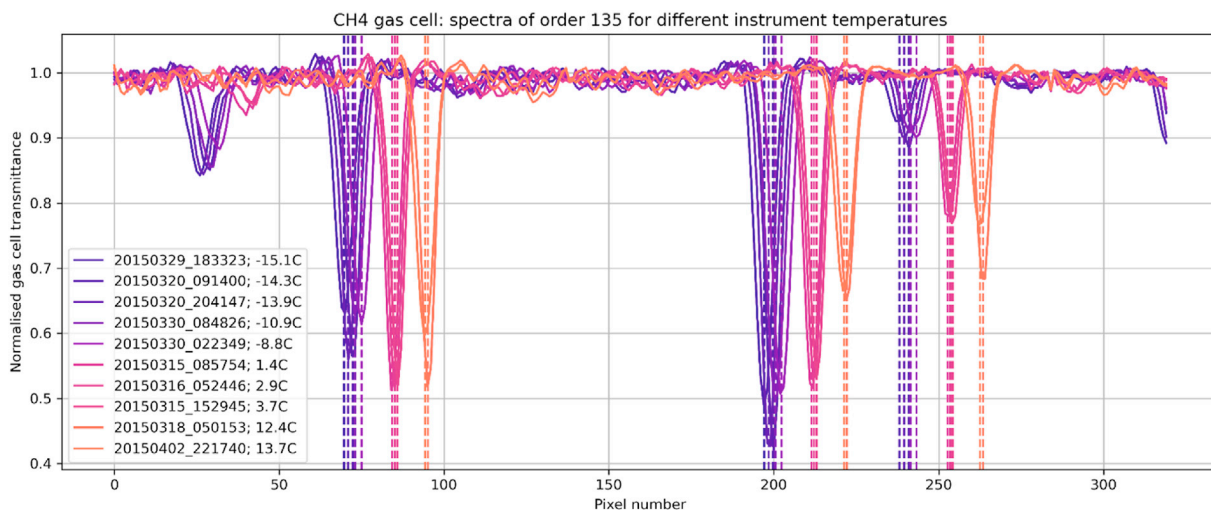


Fig. 10. Diffraction order 135 ($3035\text{-}3059\text{ cm}^{-1}$) spectra of the CH₄ gas cell measured at different instrument temperatures. The spectra have been converted to transmittance by removing the continuum, and the absorption line minima locations have been highlighted with vertical lines. The colour of the spectra denotes the instrument temperature, where orange is hotter than purple. The positions of the absorptions shift to higher pixels as the instrument gets hotter.

aluminium (6061-T6) diffraction grating expands with increasing temperature, reducing the number of lines per millimetre and therefore changing the wavelength of radiation reaching each pixel.

During ground calibration, LNO gas cell measurements were repeated five times, each at a different instrument temperature setpoint between $-15\text{ }^{\circ}\text{C}$ and $+15\text{ }^{\circ}\text{C}$. Diffraction order stepping measurements were made at each temperature of the four gas cells (CH_4 , C_2H_2 , CO_2 and CO), which were chosen to cover the spectral range of the infrared channels. The shift of each gas cell absorption position with temperature can then be quantified, as shown for diffraction order 135 in Fig. 10. The pixel shift varies linearly with temperature, and the gradient was found from a linear fit, in pixels per degree, for every absorption line in every order. The study was then repeated on the LNO inflight calibration measurements (Fig. 11), calculating the temperature shift gradient of the solar absorption lines to confirm that the results were consistent. The slope of the pixel shift vs. temperature relation is linear and consistent across all orders: the mean gradient was found to be 0.83 pixels per degree for (Fig. 12). Taking order 167 as an example, the spectral sampling (i.e. the difference in wavenumber between adjacent pixels) is 0.1 cm^{-1} , and the temperature shift for this order is $0.077\text{ cm}^{-1}/^{\circ}\text{C}$. Ultimately the accuracy of the spectral calibration depends on how the measured LNO channel temperature reflects the real temperature of the diffraction grating: when comparing many spectra across a wide temperature range, as in Figs. 10 and 11, this uncertainty cancels out. For a single nadir spectrum however, the difference between the pixel position of an absorption line and the position calculated from the temperature shift typically varies in the range ± 1 pixel. For order 167, this equates to a temperature uncertainty of $1.2\text{ }^{\circ}\text{C}$ or wavenumber uncertainty of 0.1 cm^{-1} , slightly smaller than the calculated detector smile of 1.25 pixels.

5.7. Radiometric calibration

The throughput of the instrument depends on the transmission properties of the optics, the passband of the AOTF, the blaze angle of the diffraction grating and the sensitivity of the detector. Radiation enters the LNO nadir aperture, passes through the optical chain and then hits the detector, generating a signal proportional to the incident radiation. The calculation is complicated by the presence of the AOTF - which

allows some radiation from adjacent diffraction orders to reach the detector - and the temperature-dependent nature of the diffraction grating, which means that the measured spectrum changes as the instrument temperature increases or decreases.

The radiometric calibration presented here converts the raw signal into calibrated units, incorporating the effects of instrument temperature, whilst avoiding making assumptions about the AOTF or blaze functions. The blaze and AOTF can then be defined independently from the calibration, and these parameters can be incorporated into the forward model during the retrieval process, as is performed for SO channel solar occultation measurements (e.g. Aoki et al., 2019; Vandaele et al., 2019 etc.).

5.7.1. Reflectance factor conversion

Reflectance factor (REFF) is calculated using the solar calibrations, where the LNO occultation channel is pointed at the Sun and multiple spectra are taken of all diffraction orders in the LNO channel spectral range. At the time of writing, six solar calibrations have been performed so far, each at a different instrument temperature, and therefore we have a range of temperature-dependent spectra available to analyse. If the temperature of the instrument is exactly equal in both nadir and solar measurements, the conversion to reflectance factor is simple:

$$REFF = \pi \frac{ADU_{nadir}(T)}{ADU_{solar}(T) S \cos(SZA)} \quad (1)$$

Where ADU is the analogue-to-digital units (counts) of the nadir and solar observations at instrument temperature T, normalised to counts per pixel per second; SZA is the solar zenith angle of the nadir observation; and S is the solar-to-nadir scaling factor. This last parameter is calculated as:

$$S = \pi \left(\frac{r_{sun}}{d_{sun}} \right)^2 \quad (2)$$

Where r_{sun} is the radius of the Sun and d_{sun} is the distance between the Sun and Mars (accounting for the non-circular orbit of Mars around the Sun). The LNO nadir field of view sweeps across the surface of Mars as TGO moves, and therefore the real zenith angle will change during the acquisition of a nadir spectrum. The SZA used here is calculated as the

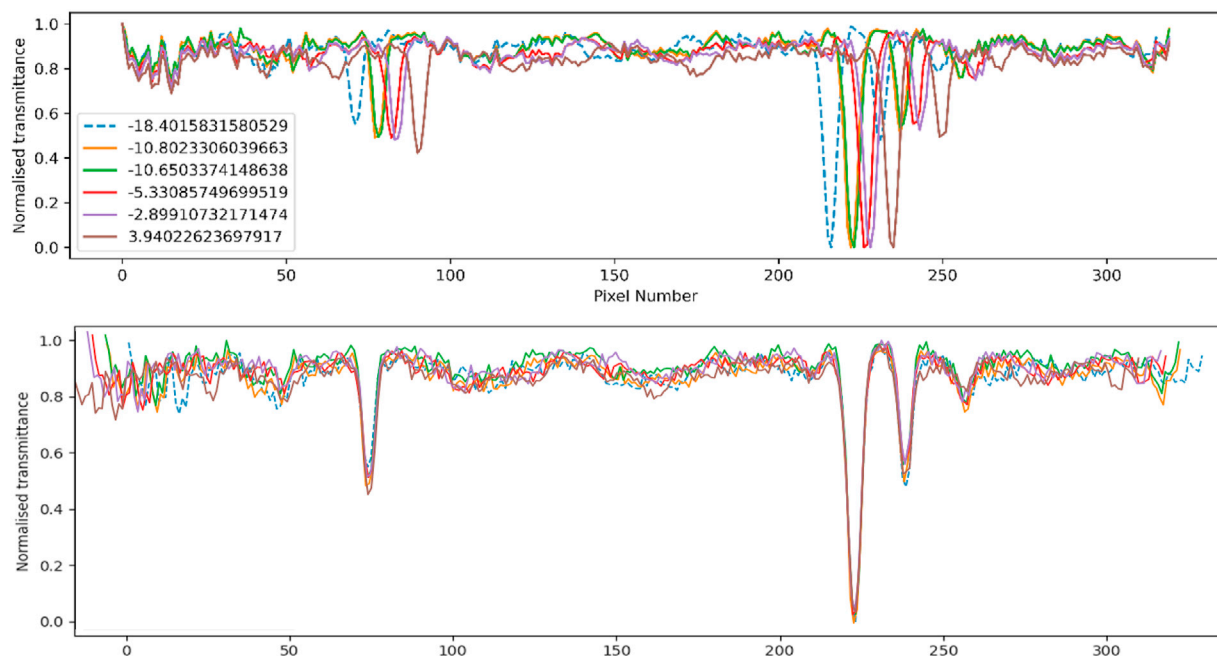


Fig. 11. Continuum-normalised diffraction order 142 ($3192\text{--}3217\text{ cm}^{-1}$) spectra of the Sun, measured at different instrument temperatures (where the temperature is given in the legend). The solar line absorptions are shown before (top) and after (bottom) the temperature shift has been corrected.

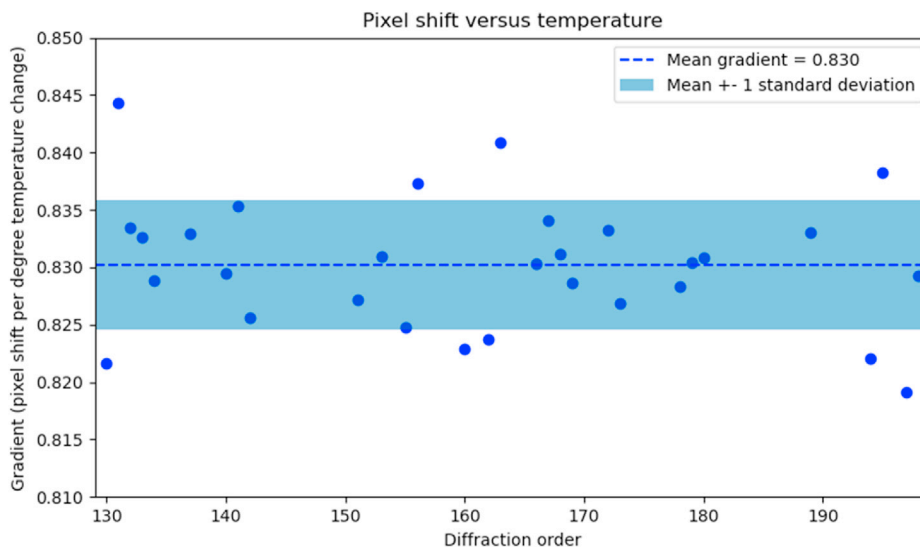


Fig. 12. Temperature shift gradients as a function of diffraction order for gas cell and solar absorption lines. The relationship is linear; the gradient does not change with diffraction order and has a 1-sigma uncertainty of 0.005 pixel/°C.

mean of the real incidence angle (taking into account surface slopes) of ten points: the centre and the four corners of the FOV at the start and end of the acquisition.

From equation (1) above, the reflectance factor calculation requires a solar spectrum measured in the same conditions as each nadir observation. Observing the raw data (e.g. Figs. 10 and 11), it is clear that the absorption lines shift on the detector as the instrument temperature changes. The LNO channel can typically be any temperature between -15C and +5C during a nadir observation, and so there are insufficient solar observations to cover all possible temperatures. Therefore, we use all the solar spectra available, taken at different temperatures, and interpolate between them to create a synthetic solar spectrum for any instrument temperature. By using the LNO data itself to calibrate the channel, we can be sure that instrumental effects, such as temperature, are accounted for in the calibration. The LNO solar spectra are acquired using the calibration mode (final row in Table 1) which returns each pixel value individually, without binning. Only the centre lines on the detector are considered, where the fields of view are centred on the Sun and are

fully encompassed by the solar disk; this is done so that the spectra are independent of the Sun-Mars distance, which changes throughout the mission. The detector sensitivity has been constant throughout the mission – further analysis of this can be found in the companion paper (Cruz-Mermy et al., 2021, this issue).

To calculate the reflectance factor, first the spectral calibration (Liuzzi et al., 2019) is first applied to the raw solar calibration data and the temperature-induced spectral shift derived from the results above. As this step uses the instrument temperature - recorded by a temperature sensor - to calculate the spectral shift, the calibration here can be incorrect by a ±1 pixel (e.g. Fig. 13, upper). This is improved by finding the positions of the known solar line minima in the spectra and shifting the spectra accordingly (Fig. 13, lower). However, obviously this can only be applied to orders where solar lines are present: in other orders the improved fit cannot be performed and the calculated spectral shift is assumed to be correct. Once the solar spectra are spectrally calibrated, the solar ADU counts are interpolated with respect to temperature for every wavenumber (Fig. 14), to make a synthetic solar spectrum for the same

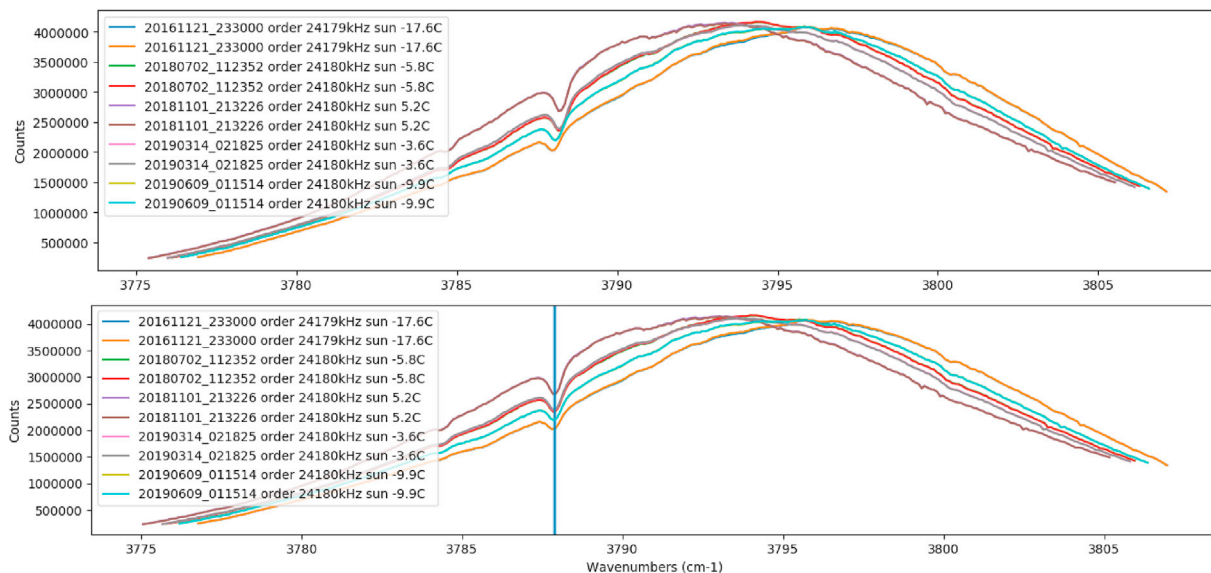


Fig. 13. LNO spectra of the Sun for diffraction order 168. Top: the spectral calibration is calculated from the instrument temperature: the solar line absorption minima are not perfectly aligned. Bottom: the spectra are shifted so that solar line minima are all on the correct wavenumber.

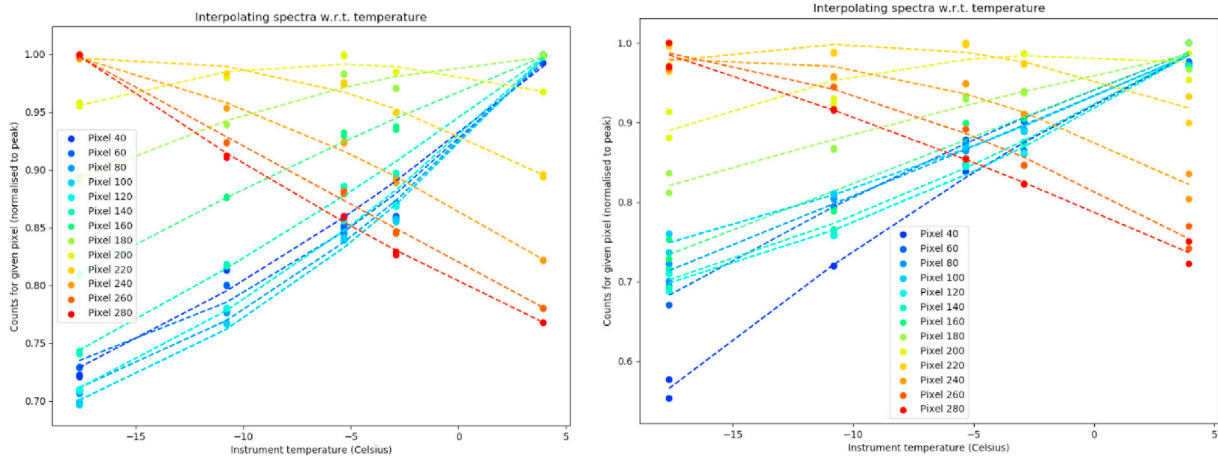


Fig. 14. For each pixel, the shift-corrected LNO solar spectra taken at different temperatures are fit with a quadratic curve with respect to the instrument temperature. This is performed for every pixel in all diffraction orders, so that a synthetic solar spectrum can be constructed for any instrument temperature. The left and right figures show the polynomial fits for two different diffraction orders: the curves here have been normalised to 1 so all the fits are visible.

instrument temperature of the nadir observation.

Next, the same principle is applied to the nadir data: the approximate spectral calibration is calculated from the instrument temperature, which is then improved by fitting to solar and/or molecular absorption lines in the spectra for those orders that contain such absorptions (Fig. 15, C). The quality of the LNO dayside nadir data varies depending on the measurement parameters used and the solar zenith angle, which varies from 0 to 90° as the TGO orbit precesses. Also, within an observation, the solar zenith angle changes as the observation begins at high northern/southern latitudes, crosses the equator, and ends at high southern/northern latitudes. If the data are too noisy, the absorption line fit will be poor, and therefore the spectral calibration could be shifted away from the correct value, and be worse than the calculated values. To avoid this,

firstly, we average together the best nadir spectra of the observation, selecting only those spectra where the ADU counts are above a defined value for that diffraction order. Then the solar and/or molecular absorptions are found in the averaged nadir spectrum, using another fit criterion to choose only those absorptions with depths greater than N standard deviations from the noise of the continuum. Two further selection criteria also ensure that only the best solar and/or molecular lines are used for the fit: one defines the minimum depth of the solar and/or molecular lines, as some orders contain many lines, and so we choose only the most prominent lines for the fit. The second defines the minimum ADU nadir counts of the continuum at the position of the absorption line, to avoid absorption lines observed at the edges of the detector where the signal is lowest, particularly pixels 0–50 and 300–320.

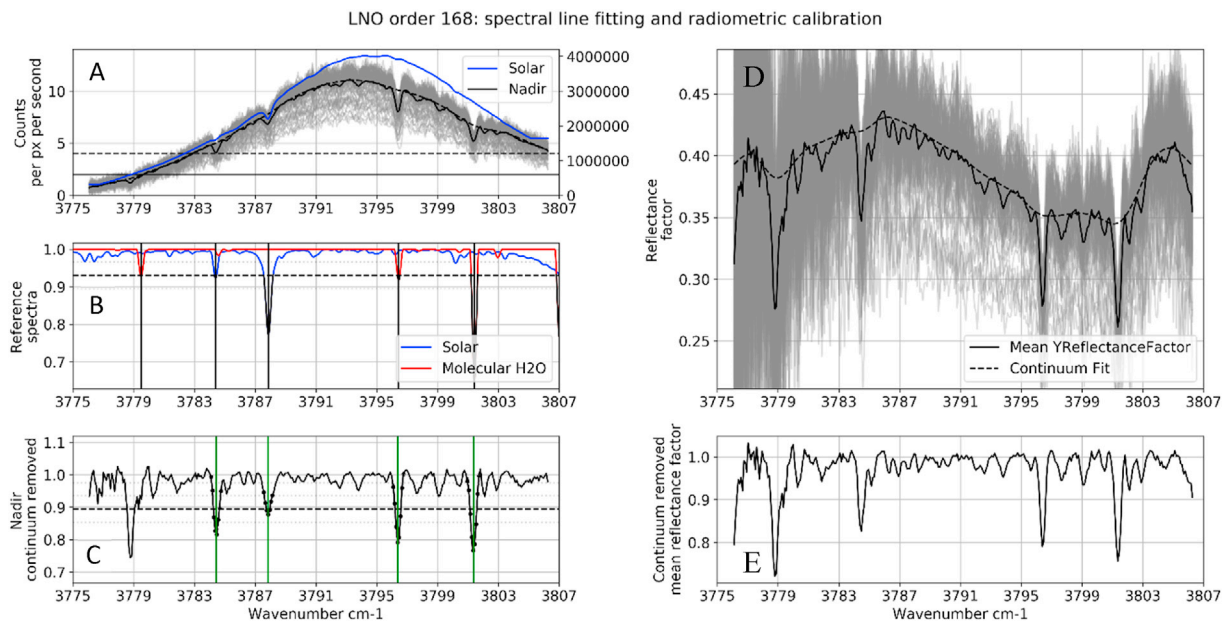


Fig. 15. Reflectance factor conversion steps for a single LNO nadir observation. [A]: The spectra are normalised to raw counts per pixel per second. Those with the highest SNR are averaged together to make a mean spectrum (solid black line) and a synthetic solar spectrum is created for same the instrument temperature (blue line). The nadir continuum is fit (dotted black line) and divided to produce a nadir flattened spectrum (C, black line). [B]: simulated reference molecular (red) and solar spectra (blue) are analysed to find the wavenumbers of possible absorption lines (black vertical lines). [C]: Observable absorption lines outside the noise level are found in the mean nadir flattened spectrum (green vertical lines). The nadir spectra are shifted so that the detected absorption lines match the simulated spectra. [D]: the shift-corrected nadir spectra are divided by the solar spectra and variables in Equation (1) to convert to reflectance factor (grey lines). [E]: an example of the mean reflectance factor spectrum once the continuum has been removed. The main solar line at 3788 cm⁻¹ has been suppressed by the conversion to reflectance factor.

In cases where the fitting fails, that particular absorption is discarded. If no lines can be fit, either because the fit fails or the criteria above are not satisfied, then the pre-calculated spectral calibration using the instrument temperature is kept unchanged (however if the spectra are noisy, so that absorption lines are not detectable, the spectral calibration is less critical anyway). This happens particularly for orders 115–155, where the instrument sensitivity is lower (e.g. the inverse of Fig. 9, and see the companion paper, Cruz-Mermy et al., 2021, this issue) or when the viewing conditions are not favourable (e.g. high solar zenith angles). For diffraction orders 167–169 (H₂O lines), ~90% of observations are correctly fitted; for orders 189–190 (CO lines), ~75% are fitted. The spectra are converted to reflectance factor using equation (1) (Fig. 15, D). To see the relative depths of the absorption lines, a continuum removal technique – here Eilers and Boelens (2005) – is applied to flatten the continuum (Fig. 15, E); however this removes broader surface features from the spectra.

Uncertainties can be divided into systematic and random: the former describes the absolute precision between the actual value and that measured, whereas the latter describes the relative precision from the mean measured value i.e. the SNR. Following the radiometric calibration procedure described above, it is clear that some steps will contribute more to the total uncertainty than others.

The radiometric calibration uses data acquired by the LNO channel to calibrate the LNO nadir data, which minimises any systematic optical or detector effects. The SZA in equation (1) is calculated with SPICE kernels (Acton, 1996) from the reconstructed TGO orbit, and a 4 pixel per degree digital shape kernel is used to accurately determine the angle between Sun and the mean slope of the surface being observed, giving the most accurate value possible. An error of even 1° in SZA would only give a small bias to the reflectance factor: for example the relative percentage difference between $\cos(45^\circ)$ and $\cos(44^\circ)$ is 1.7%, and less for smaller angles. Variables such as the Sun-Mars distance and the solar radius in equation (2) are known very accurately. The LNO boresight points ~20 arcminutes from the TGO nadir-pointing axis, so there is no effect due to off-nadir pointing. There is however a small systematic error introduced by the interpolation of the solar spectra (Fig. 14). The maximum deviation of the points from the fit is ~2%, which would cause a systematic error of the same magnitude for that pixel.

The SNRs of the solar observations are very high (>1000) and therefore have a negligible impact on the random error. Instead, the main source of error is the low SNR of the nadir observations, which varies according to many factors. The noise level depends on the instrument temperature (smaller thermal background when cold). The signal level depends on: (a) the solar zenith angle (less incident flux from oblique angles), (b) the diffraction order (instrument is most sensitive in orders 165–190; Fig. 9), (c) the number of diffraction orders measured (total observation time per spectrum is smaller when more orders are measured; Table 1 column 3), and (d) the position on detector (signal is higher on the central columns of the detector due to the AOTF and blaze functions).

In total, the maximum expected systematic error would therefore be around 4%, and the maximum random error would depend on the many observation parameters described above. A simple example SNR calculation can give an approximation: first, the random noise is taken from nadir observations made on the nightside of the planet. The standard deviation when NOMAD is at -10C is $\sim 125 \pm 10$ counts. A typical spectrum of order 167, for an observation with 3 diffraction orders and an SZA of 20° has ~3000 counts at the centre of the detector, and so the SNR would be ~25 for this observation (this can be increased considerably by binning multiple spectra together). This value is approximately as expected from theoretical models (Thomas et al., 2016), who calculated an expected SNR of 100–150 for a 15s observation in good observing conditions. With background subtraction enabled (50% observation time lost) and 3 diffraction orders measured (i.e. 5 s each), the effective SNR should be 17–25, which agrees with the simple calculation above.

An accompanying paper (Cruz-Mermy et al., 2021, this issue) investigated the LNO radiometric calibration in more detail, approaching the work from a theoretical perspective. This companion paper started from first principles, modelling the instrument response, checking calibration stability over time and investigating instrument temperature effects. Both analyses agree within 3% of each other, demonstrating a good validation of each method. Other results also agree between the two papers, such as the temperature-induced pixel shift, even though the two calibration methods have different approaches.

The LNO calibration here includes no correction to the continuum shape, and hence all surface, cloud and atmospheric features are preserved in the data. The companion paper analysis (Cruz-Mermy et al., 2021, this issue) uses a continuum removal technique to flatten the spectra, and the results confirm that when the LNO blaze and AOTF functions are simulated and the derived ILS is used, the resulting continuum-removed solar spectra match well with simulations. To use the dataset presented in this work for atmospheric retrievals, such as for fitting to H₂O or CO lines, a continuum removal method e.g. (Eilers and Boelens, 2005) should be used to remove the effects of the surface and dust/aerosols from the spectra. The method of Cruz-Mermy et al. (2021), (this issue) uses a continuum removal method as part of the calibration procedure, therefore broad spectral shapes such as surface features are already flattened.

5.7.2. Applications

With all LNO data converted to reflectance factor, further analysis can be performed such as molecular retrievals, dust/opacity studies and surface composition studies. The reflectance factor data presented here was used to derive maps of the CO distribution (Smith et al., 2021). This dataset can also be used for water vapour distribution studies.

By removing the molecular absorption lines and calculating the mean continuum reflectance factor of each LNO nadir spectrum, a map of surface reflectance can be produced such as that shown in Fig. 16. The resulting map matches the TES albedo map well, once a correction has been applied to the TES data to convert the bolometric albedo values to reflectance factor albedo at the wavelength of the chosen diffraction order. This correction is derived from a comparison of TES and OMEGA data of the same spectral range, where reflectance factor for order 167 is approximately equal to 0.7 x bolometric albedo [G. Bellucci, personal communication]. The good match between the two, once this scaling factor is applied, shows that the calibrated reflectance factors derived here are in accordance with the expected values.

6. Conclusions

Calibration of the NOMAD nadir channels was the highest priority before launch, as these channels are not self-calibrating like the SO, LNO and UVIS occultation channels. From ground and in-flight observations, both the LNO nadir and occultation channels have been successfully calibrated, including detector characterisation, boresight pointing direction, and spectral and radiometric calibration. An accompanying paper, part 1, addresses similar calibration aspects for SO, the other infrared channel in NOMAD (Thomas et al., 2021, this issue).

The results from the first Martian year of calibration activities are presented here. Firstly, the nadir and occultation boresight pointing directions have been determined. The occultation boresight, which must be known to within ~1–2 arcminutes for solar occultations, was found from solar FOV scans - where the spacecraft is slewed around the solar disk and the illumination pattern on the detector is recorded. From the illumination patterns, the central detector row and extent of the illuminated region was also found; this analysis is valid for both nadir and solar occultation modes equally. The nadir boresight, which could not be pointed towards the Sun, was instead found from scanning across the sunlit limb of the planet. Accuracy here is less important, as in nadir mode the boresight is used only to calculate the observing geometry e.g. the surface latitude and longitude. Integration times for both nadir and

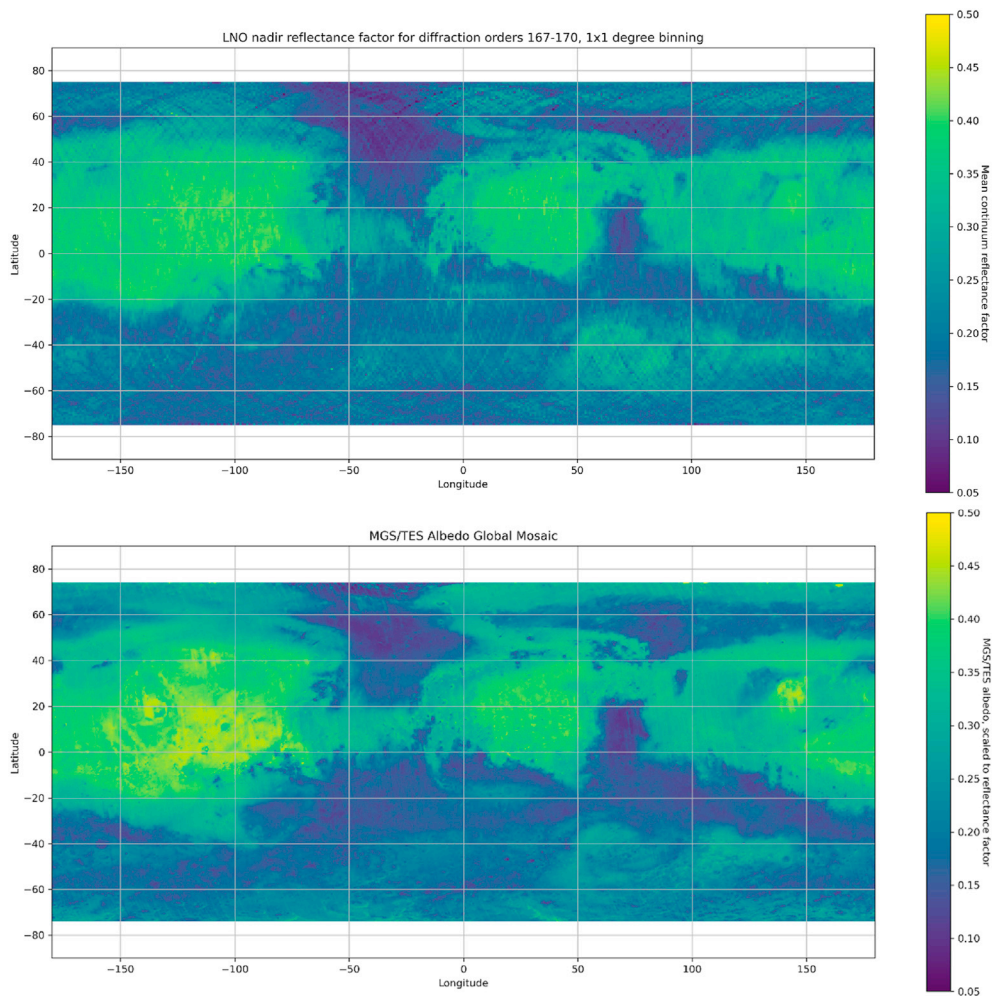


Fig. 16. Top: LNO continuum level for diffraction orders 167–170 (those typically used for H₂O mapping), binned onto a 1° × 1° grid. The surface albedo map matches well to the TES bolometric albedo map (bottom).

solar occultations were calculated, and bad detector pixels identified. The spectra recorded in-flight are regularly checked for the presence of additional bad pixels not detected in the ground calibration data. The extent of detector smile was also examined. The spectral calibration of each pixel changes as the instrument temperature changes – this temperature-induced pixel shift was determined, which is important to calibrate the wavenumber of each pixel in each diffraction order. This result was confirmed in a companion paper (Cruz-Mermey et al., 2021, this issue).

The LNO nadir channel was radiometrically calibrated, using multiple solar observations recorded by the channel itself. The instrument temperature was incorporated into the calibration, so that temperature differences between the nadir and solar data did not introduce errors. An accompanying paper (Cruz-Mermey et al., 2021, this issue) investigated the LNO radiometric calibration from a theoretical perspective: the two analyses agree within 3% of each other, as shown in the companion paper, demonstrating a good validation of each method. The companion paper analysis (Cruz-Mermey et al., 2021, this issue) uses a continuum removal technique to flatten the spectra, removing broad spectral features such as those caused by surface composition, ice or dust/aerosols. These features are retained in the LNO nadir calibration dataset presented in this work, so for retrievals of atmospheric gases (e.g. H₂O or CO) either a continuum removal method should be applied to the nadir spectra to flatten the spectra (Smith et al., 2021), or surface and dust/aerosol spectral features should be incorporated into the retrieval forward model. Conversely, the spectra of (Cruz-Mermey et al., 2021, this

issue) can be used directly for retrievals of atmospheric gases but not for analysis of other spectral features.

7. Data availability

At the time of writing, SO occultation and UVIS occultation and nadir calibrated datasets are available on the ESA Planetary Science Archive (Besse et al., 2018) at <https://psa.esa.int/> for all data since the beginning of the nominal science mission (21st April 2018) up to 2020, with more recent data delivered regularly. LNO, UVIS limb, and calibration datasets for all channels are under preparation and are expected to be released to the public soon. The peer-reviewed EAICD (experiment-to-archive interface document), written by the lead author of this work, is available on the ESA PSA and describes the data archived there in much more detail.

Funding

This project acknowledges funding by the Belgian Science Policy Office (BELSPO), with the financial and contractual coordination by the ESA Prodex Office (PEA 4000103401, 4000121493), by Spanish Ministry of Science and Innovation (MCIU) and by European funds under grants PGC2018-101836-B-I00 and ESP2017-87143-R (MINECO/FEDER), as well as by the UK Space Agency through grants ST/V002295/1, ST/V005332/1 and ST/S00145X/1 and ST/R001405/1 and Italian Space Agency through grant 2018-2-HH.0. This work was supported by the

Belgian Fonds de la Recherche Scientifique – FNRS under grant number 30442502 (ET_HOME). The IAA/CSIC team acknowledges financial support from the State Agency for Research of the Spanish MCIU through the ‘Center of Excellence Severo Ochoa’ award for the Instituto de Astrofísica de Andalucía (SEV-2017-0709). SR thanks BELSPO for the FED-tWIN funding (Prf-2019-077 - RT-MOLEXO).

Author statement

Ian R. Thomas: Conceptualization, Methodology, Software, Validation, Investigation, Writing, Visualization.

Shohei Aoki: Investigation, Software, Formal analysis.

Loïc Trompet: Investigation, Formal analysis.

Séverine Robert: Investigation.

Cédric Depiesse: Investigation.

Yannick Willame: Investigation.

Guillaume Cruz-Mermy: Validation.

Frédéric Schmidt: Validation, Supervision.

Justin T. Erwin: Investigation, Formal analysis.

Ann Carine Vandaele: Investigation, Conceptualization, Supervision, Funding acquisition.

Frank Daerden: Investigation.

Arnaud Mahieux: Investigation.

Eddy Neefs: Investigation, Conceptualization, Supervision.

Bojan Ristic: Investigation, Validation.

Laszlo Hetey: Project administration.

Sophie Berkenbosch: Software, Data Curation.

Roland Clairquin: Software, Data Curation.

Bram Beeckman: Software, Data Curation.

Manish R. Patel: Investigation, Conceptualization, Supervision.

Jose Juan Lopez-Moreno: Conceptualization, Supervision.

Giancarlo Bellucci: Conceptualization, Supervision.

Declaration of competing interest

The authors declare that they have no known competing financial interests or personal relationships that could have appeared to influence the work reported in this paper.

Acknowledgements

The NOMAD experiment is led by the Royal Belgian Institute for Space Aeronomy (BIRA-IASB), assisted by Co-PI teams from Spain (IAA-CSIC), Italy (INAF-IAPS), and the United Kingdom (Open University). We would like to thank everyone involved in the ExoMars project.

References

- Acton, C.H., 1996. Ancillary data services of NASA's navigation and Ancillary Information Facility. *Planet. Space Sci.* 44. [https://doi.org/10.1016/0032-0633\(95\)00107-7](https://doi.org/10.1016/0032-0633(95)00107-7).
- Aoki, S., Vandaele, A.C., Daerden, F., Villanueva, G.L., Liuzzi, G., Thomas, I.R., Erwin, J.T., Trompet, L., Robert, S., Neary, L., Viscardy, S., Clancy, R.T., Smith, M.D., Lopez-Valverde, M.A., Hill, B., Ristic, B., Patel, M.R., Bellucci, G., Lopez-Moreno, J.J., Alonso-Rodrigo, G., Altieri, F., Bauduin, S., Bolsée, D., Carozzo, G., Cloutis, E., Crismani, M., Da Pieve, F., D'aversa, E., Depiesse, C., Etiopie, G., Fedorova, A.A., Funke, B., Fussen, D., Garcia-Comas, M., Geminale, A., Gérard, J.C., Giuranna, M., Gkouvelis, L., Gonzalez-Galindo, F., Holmes, J., Hubert, B., Ignatiev, N.I., Kaminski, J., Karatekin, O., Kasaba, Y., Kass, D., Kleinböhl, A., Lanciano, O., Lefèvre, F., Lewis, S., López-Puertas, M., López-Valverde, M., Mahieux, A., Mason, J., Mege, D., Mumma, M.J., Nakagawa, H., Neefs, E., Novak, R.E., Oliva, F., Piccialli, A., Renotte, R., Ritter, B., Schmidt, F., Schneider, N., Sindoni, G., Teanby, N.A., Thiemann, E., Trokhimovskiy, A., Auwera, Vander, J., Whiteway, J., Wilquet, V., Willame, Y., Wolff, M.J., Wolkenberg, P., Yelle, R., Del Moral Beatriz, A., Barzin, P., Beeckman, B., Benmoussa, A., Berkenbosch, S., Biondi, D., Bonnewijn, S., Candini, G.P., Clairquin, R., Cubas, J., Giordanengo, B., Gissot, S., Gomez, A., Hathi, B., Jeronimo Zafra, J., Leese, M., Maes, J., Mazy, E., Mazzoli, A., Meseguer, J., Morales, R., Orban, A., Pastor-Morales, M., Perez-Grande, I., Queirolo, C., Rodriguez Gomez, J., Saggin, B., Samain, V., Sanz Andres, A., Sanz, R., Simar, J.F., Thibert, T., 2019. Water vapor vertical profiles on Mars in dust storms observed by TGO/NOMAD. *J. Geophys. Res. Planets* 124. <https://doi.org/10.1029/2019JE006109>.

- Besse, S., Vallat, C., Barthelemy, M., Coia, D., Costa, M., De Marchi, G., Fraga, D., Grotheer, E., Heather, D., Lim, T., Martinez, S., Arviset, C., Barbarisi, I., Docasal, R., Macfarlane, A., Rios, C., Saiz, J., Vallejo, F., 2018. ESA's Planetary Science Archive: preserve and present reliable scientific data sets. *Planet. Space Sci.* 150, 131–140. <https://doi.org/10.1016/j.pss.2017.07.013>.
- Cruz-Mermy, G., Schmidt, F., Thomas, I.R., Daerden, F., Ristic, B., Patel, M.R., Lopez-Moreno, J.-J., Bellucci, G., Vandaele, A.C., 2021. Calibration of NOMAD on ExoMars trace gas orbiter: Part 3 – LNO validation and instrument stability. *Planet. Space Sci.* (this issue).
- Eilers, P.H., Boelens, H.F., 2005. Baseline correction with asymmetric least squares smoothing. *Leiden University Medical Centre Report 1* (1), 5.
- Korablev, O., Olsen, K.S., Trokhimovskiy, A., Lefèvre, F., Montmessin, F., Fedorova, A.A., Toplis, M.J., Alday, J., Belyaev, D.A., Patrakeeve, A., Ignatiev, N.I., Shakun, A.V., Grigoriev, A.V., Baggio, L., Abdenour, I., Lacombe, G., Ivanov, Y.S., Aoki, S., Thomas, I.R., Daerden, F., Ristic, B., Erwin, J.T., Patel, M., Bellucci, G., Lopez-Moreno, J.J., Vandaele, A.C., 2021. Transient HCl in the atmosphere of Mars. *Sci. Adv.* 7, 4386. <https://doi.org/10.1126/sciadv.abe4386>.
- Liuzzi, G., Villanueva, G.L., Crismani, M.M.J., Smith, M.D., Mumma, M.J., López-Valverde, F., Aoki, S., Vandaele, A.C., Clancy, R.T., Erwin, J., Thomas, I., Ristic, B., Lopez-Moreno, J.J., Bellucci, G., Patel, M.R., 2020. Strong variability of martian water ice clouds during dust storms revealed from ExoMars trace gas orbiter/NOMAD. *J. Geophys. Res. Planets* 125. <https://doi.org/10.1029/2019JE006250>.
- Liuzzi, G., Villanueva, G.L., Mumma, M.J., Smith, M.D., Daerden, F., Ristic, B., Thomas, I., Vandaele, A.C., Patel, M.R., Lopez-Moreno, J.J., Bellucci, G., Allen, M., Alonso-Rodrigo, G., Altieri, F., Aoki, S., Bauduin, S., Bolsée, D., Clancy, T., Cloutis, E., D'Aversa, E., Depiesse, C., Erwin, J., Fedorova, A., Formisano, V., Funke, B., Fussen, D., Garcia-Comas, M., Geminale, A., Gérard, J.C., Gillotay, D., Giuranna, M., Gonzalez-Galindo, F., Hewson, W., Homes, J., Ignatiev, N., Kaminski, J., Karatekin, O., Kasaba, Y., Lanciano, O., Lefèvre, F., Lewis, S., López-Puertas, M., López-Valverde, M., Mahieux, A., Mason, J., Mc Connell, J., Hiromu Neary Nakagawa, L., Neefs, E., Novak, R., Oliva, F., Piccialli, A., Renotte, E., Robert, S., Sindoni, G., Stiepen, A., Trokhimovskiy, A., Vander Auwera, J., Viscardy, S., Whiteway, J., Willame, Y., Wilquet, V., Wolff, M., Wolkenberg, P., Alonso-Rodrigo, G., Aparicio del Moral, B., Barzin, P., Beeckman, B., BenMoussa, A., Berkenbosch, S., Biondi, D., Bonnewijn, S., Candini, G.P., Clairquin, R., Cubas, J., Giordanengo, B., Gissot, S., Gomez, A., Hathi, B., Jeronimo Zafra, J., Leese, M., Maes, J., Mazy, E., Mazzoli, A., Meseguer, J., Morales, R., Orban, A., Pastor-Morales, M., Perez-grande, I., Queirolo, C., Rodriguez Gomez, J., Saggin, B., Samain, V., Sanz Andres, A., Sanz, R., Simar, J.F., Thibert, T., 2019. Methane on Mars: new insights into the sensitivity of CH₄ with the NOMAD/ExoMars spectrometer through its first in-flight calibration. *Icarus* 321. <https://doi.org/10.1016/j.icarus.2018.09.021>.
- Neefs, E., Vandaele, A.C., Drummond, R., Thomas, I.R., Berkenbosch, S., Clairquin, R., Delanoye, S., Ristic, B., Maes, J., Bonnewijn, S., Pieck, G., Equeter, E., Depiesse, C., Daerden, F., Ransbeeck, Van, E., Nevejans, D., Rodriguez-Gómez, J., López-Moreno, J.-J., Sanz, R., Morales, R., Candini, G.P., Carmen Pastor-Morales, M., Aparicio, B., Moral, D., Jeronimo-Zafra, J.-M., Manuel Gómez-López, J., Alonso-Rodrigo, G., Pérez-Grande, I., Cubas, J., Gomez-Sanjuan, A.M., Navarro-Medina, F., Thibert, T., Patel, M.R., Bellucci, G., De Vos, L., Lesschaeve, S., Kendall, D., De Neef, J., Soenen, A., Puech, P.-Y., Ward, J., Jamoye, J.-F., Diez, D., Vicario-Arroyo, A., Jankowski, M., 2015. NOMAD Spectrometer on the ExoMars Trace Gas Orbiter Mission: Part 1—design, Manufacturing and Testing of the Infrared Channels. <https://doi.org/10.1364/AO.54.008494>.
- Patel, M.R., Antoine, P., Mason, J., Leese, M., Hathi, B., Stevens, A.H., Dawson, D., Gow, J., Ringrose, T., Holmes, J., Lewis, S.R., Beghuni, D., van Doninck, P., Ligot, R., Dewandel, J.-L., Hu, D., Bates, D., Cole, R., Drummond, R., Thomas, I.R., Depiesse, C., Neefs, E., Equeter, E., Ristic, B., Berkenbosch, S., Bolsée, D., Willame, Y., Vandaele, A.C., Lesschaeve, S., De Vos, L., Van Vooren, N., Thibert, T., Mazy, E., Rodriguez-Gomez, J., Morales, R., Candini, G.P., Pastor-Morales, M.C., Sanz, R., Aparicio del Moral, B., Jeronimo-Zafra, J.-M., Gómez-López, J.M., Alonso-Rodrigo, G., Pérez-Grande, I., Cubas, J., Gomez-Sanjuan, A.M., Navarro-Medina, F., BenMoussa, A., Giordanengo, B., Gissot, S., Bellucci, G., Lopez-Moreno, J.J., 2017. NOMAD spectrometer on the ExoMars trace gas orbiter mission: part 2—design, manufacturing, and testing of the ultraviolet and visible channel. *Appl. Opt.* 56. <https://doi.org/10.1364/ao.56.002771>.
- Smith, M.D., Daerden, F., Neary, L., Khayat, A.S.J., Holmes, J.A., Patel, M.R., Villanueva, G., Liuzzi, G., Thomas, I.R., Ristic, B., Bellucci, G., Lopez-Moreno, J.J., Vandaele, A.C., 2021. The climatology of carbon monoxide on Mars as observed by NOMAD nadir-geometry observations. *Icarus* 114404. <https://doi.org/10.1016/j.icarus.2021.114404>.
- Thomas, I.R., Aoki, S., Trompet, L., Robert, S., Depiesse, C., Willame, Y., Erwin, J.T., Vandaele, A.C., Daerden, F., Mahieux, A., Neefs, E., Ristic, B., Hetey, L., Berkenbosch, S., Clairquin, R., Beeckman, B., Patel, M.R., Lopez-Moreno, J.J., Bellucci, G., 2021. Calibration of NOMAD on ExoMars trace gas orbiter: Part 1 – the SO channel. *Planet. Space Sci.* (this issue).
- Thomas, I.R., Vandaele, A.C., Robert, S., Neefs, E., Drummond, R., Daerden, F., Delanoye, S., Ristic, B., Berkenbosch, S., Clairquin, R., Maes, J., Bonnewijn, S., Depiesse, C., Mahieux, A., Trompet, L., Neary, L., Willame, Y., Wilquet, V., Nevejans, D., Aballea, L., Moelans, W., De Vos, L., Lesschaeve, S., Van Vooren, N., Lopez-Moreno, J.-J., Patel, M.R., Bellucci, G., the NOMAD Team, 2016. Optical and radiometric models of the NOMAD instrument part II: the infrared channels - SO and LNO. *Opt Express* 24. <https://doi.org/10.1364/oe.24.003790>.
- Trompet, L., Mahieux, A., Ristic, B., Robert, S., Wilquet, V., Thomas, I.R., Vandaele, A.C., Bertaux, J.-L., 2016. Improved algorithm for the transmittance estimation of spectra

- obtained with SOIR/Venus Express. *Appl. Opt.* 55, 9275. <https://doi.org/10.1364/ao.55.009275>.
- Vandaele, A.C., Korabiev, O., Daerden, F., Aoki, S., Thomas, I.R., Altieri, F., López-Valverde, M., Villanueva, G., Liuzzi, G., Smith, M.D., Erwin, J.T., Trompet, L., Fedorova, A.A., Montmessin, F., Trokhimovskiy, A., Belyaev, D.A., Ignatiev, N.I., Luginin, M., Olsen, K.S., Baggio, L., Alday, J., Bertaux, J.L., Betsis, D., Bolsée, D., Clancy, R.T., Cloutis, E., Depiesse, C., Funke, B., Garcia-Comas, M., Gérard, J.C., Giuranna, M., Gonzalez-Galindo, F., Grigoriev, A.V., Ivanov, Y.S., Kaminski, J., Karatekin, O., Lefèvre, F., Lewis, S., López-Puertas, M., Mahieux, A., Maslov, I., Mason, J., Mumma, M.J., Neary, L., Neefs, E., Patrakee, A., Patsaev, D., Ristic, B., Robert, S., Schmidt, F., Shakun, A., Teanby, N.A., Viscardy, S., Willame, Y., Whiteway, J., Wilquet, V., Wolff, M.J., Bellucci, G., Patel, M.R., López-Moreno, J.J., Forget, F., Wilson, C.F., Svedhem, H., Vago, J.L., Rodionov, D., Alonso-Rodrigo, G., Bauduin, S., Carozzo, G., Crismani, M., Da Pieve, F., D'Aversa, E., Etiopie, G., Fussen, D., Geminale, A., Gkouvelis, L., Holmes, J., Hubert, B., Kasaba, Y., Kass, D., Kleinböhl, A., Lanciano, O., Nakagawa, H., Novak, R.E., Oliva, F., Piccialli, A., Renotte, E., Ritter, B., Schneider, N., Sindoni, G., Thiemann, E., Vander Auwera, J., Wolkenberg, P., Yelle, R., Anufreychik, K., Arnold, G., Bertaux, J.L., Duxbury, N., Fouchet, T., Grassi, D., Guerlet, S., Hartogh, P., Khatuntsev, I., Kokonkov, N., Krasnopolsky, V., Kuzmin, R., Lacombe, G., Lellouch, E., Määttä, A., Marcq, E., Martin-Torres, J., Medvedev, A., Millour, E., Moshkin, B., Patel, M.R.R., Quantin, Nataf, C., Rodin, A., Shematovich, V., Thomas, N., Trokhimovsky, A., Vazquez, L., Vincendon, M., Young, R., Zasova, L., Zelenyi, L., Zorzano, M.P., 2019. Martian dust storm impact on atmospheric H₂O and D/H observed by ExoMars Trace Gas Orbiter. *Nature* 568. <https://doi.org/10.1038/s41586-019-1097-3>.
- Vandaele, A.C., Neefs, E., Drummond, R., Thomas, I.R., Daerden, F., Lopez-Moreno, J.J., Rodriguez, J., Patel, M.R., Bellucci, G., Allen, M., Altieri, F., Bolsée, D., Clancy, T., Delanoye, S., Depiesse, C., Cloutis, E., Fedorova, A., Formisano, V., Funke, B., Fussen, D., Geminale, A., Gérard, J.C., Giuranna, M., Ignatiev, N., Kaminski, J., Karatekin, O., Lefèvre, F., López-Puertas, M., López-Valverde, M., Mahieux, A., McConnell, J., Mumma, M., Neary, L., Renotte, E., Ristic, B., Robert, S., Smith, M., Trokhimovsky, S., Vanderauwera, J., Villanueva, G., Whiteway, J., Wilquet, V., Wolff, M., Aoki, S., Garcia-Comas, M., Gillotay, D., Gonzalez-Galindo, F., Kasabe, Y., Lewis, S., Mason, J., Sindoni, G., Willame, Y., Alonso-Rodrigo, G., Aparicio Del Moral, B., Barzin, P., Ben Moussa, A., Berkenbosch, S., Biondi, D., Bonnewijn, S., Candini, G.P., Clairquin, R., Cubas, J., Giordanengo, B., Gissot, S., Gomez, A., Zafra, J.J., Leese, M., Maes, J., Mazy, E., Mazzoli, A., Meseguer, J., Morales, R., Urban, A., Pastor-Morales, M.D.C., Perez-Grande, I., Rodriguez-Gomez, J., Saggin, B., Samain, V., Sanz Andres, A., Sanz, R., Simar, J.F., Thibert, T., 2015. Science objectives and performances of NOMAD, a spectrometer suite for the ExoMars TGO mission. *Planet. Space Sci.* 119. <https://doi.org/10.1016/j.pss.2015.10.003>.